bioRxiv preprint doi: https://doi.org/10.1101/2021.03.25.436951; this version posted March 25, 2021. The copyright holder for this preprint (which was not certified by peer review) is the author/funder, who has granted bioRxiv a license to display the preprint in perpetuity. It is made available under aCC-BY 4.0 International license.

A robust, semi-automated approach for counting cementum increments imaged with X-ray computed tomography

Elis Newham[1,2*], Pamela G. Gill.[3,4], Kate Robson Brown[5,6], Neil J. Gostling[7], Ian J. Corfe[8,9], & Philipp Schneider[1*].

* Corresponding author

1. Bioengineering Science Research Group, Faculty of Engineering and Physical Sciences, University of Southampton. University Road, Southampton, SO17 1BJ, United Kingdom.
2. School of Physics, University of Bristol. HH Wills Physics Laboratory, Bristol, BS8 1TL, United Kingdom.
3. School of Earth Sciences, University of Bristol. Wills Memorial Building, Queens Road, Bristol, BS8 1RJ, United Kingdom.
4. Department of Earth Sciences, Natural History Museum. Cromwell Road, London, SW7 5BD, United Kingdom.
5. Department of Mechanical Engineering, Queen's Building, University of Bristol, Bristol, UK.
6. Department of Anthropology and Archaeology, University of Bristol. 43 Woodland Road, Bristol, BS8 1UU, United Kingdom.
7. Faculty of Environmental and Life Sciences, University of Southampton, Southampton, UK.
8. Developmental Biology Program, Institute of Biotechnology, University of Helsinki. Viikinkaari 5D, University of Helsinki, Helsinki, Finland.
9. Geological Survey of Finland, Espoo, Finland.

bioRxiv preprint doi: https://doi.org/10.1101/2021.03.25.436951; this version posted March 25, 2021. The copyright holder for this preprint (which was not certified by peer review) is the author/funder, who has granted bioRxiv a license to display the preprint in perpetuity. It is made available under aCC-BY 4.0 International license.

Abstract

Cementum, the tissue attaching mammal tooth roots to the periodontal ligament, grows appositionally throughout life, displaying a series of circum-annual incremental features. These have been studied for decades as a direct record of chronological lifespan. The majority of previous studies on cementum have used traditional thin-section histological methods to image and analyse increments. However, several caveats have been raised in terms of studying cementum increments in thin-sections. Firstly, the limited number of thin-sections and the two-dimensional perspective they impart provide an incomplete interpretation of cementum structure, and studies often struggle or fail to overcome complications in increment patterns that complicate or inhibit increment counting. Increments have been repeatedly shown to both split and coalesce, creating accessory increments that can bias increment counts. Secondly, identification and counting of cementum increments using human vision is subjective, and it has led to inaccurate readings in several experiments studying individuals of known age. Here, we have attempted to optimise a recently introduced imaging modality for cementum imaging; X-ray propagation-based phase-contrast imaging (PPCI). X-ray PPCI was performed for a sample of rhesus macaque (*Macaca mulatta*) lower first molars (n=10) from a laboratory population of known age. A new method for semi-automatic increment counting was then integrated into a purpose-built software package for studying cementum increments. Comparison with data from conventional cementochronology, based on histological examination of tissue sections, confirmed that X-ray PPCI reliably records cementum increments. Validation of the increment counting algorithm suggests that it is robust and provides accurate estimates of increment counts. In summary, we show that our new increment counting method has the potential to overcome caveats of conventional

bioRxiv preprint doi: https://doi.org/10.1101/2021.03.25.436951; this version posted March 25, 2021. The copyright holder for this preprint (which was not certified by peer review) is the author/funder, who has granted bioRxiv a license to display the preprint in perpetuity. It is made available under aCC-BY 4.0 International license.

cementochronology approaches, when used to analyse 3D images provided by X-ray PPCI.

1. Introduction

Mammalian teeth comprise three principal mineralised tissues: enamel, dentine and cementum. Each tissue provides its own record of growth via incremental patterns observed using thin-section histology that track periodic changes in their growth rates. Development of enamel and dentine is largely truncated after the maturation of the tooth. However, cementum grows continuously throughout life and provides a more complete record of an individual's life history (Klevezal, 1996). Incremental features found in cementum are well understood to have a circum-annual periodicity, with one thick translucent increment, and one thin opaque increment formed every year (when viewed in thin-section under transmitted light microscopy; Fig. 1). These contrasting opacities are hypothesised to be primarily due to seasonal changes in the mineralisation rates of the cementum hydroxyapatite matrix. Cementum is composed of bundles of collagen fibres emanating from the both the cementum itself (intrinsic fibres), or from the periodontal ligament or PDL (extrinsic 'Sharpey's' fibres), wrapped within a hydroxyapatite matrix. Unfavourable growth seasons promote a reduction in the deposition rate of this matrix, while the mineralisation rate is unaffected. This produces ultra-mineralisation of thinner portions of cementum during these periods (Lieberman, 1993; Klevezal, 1996; though see Stock et al 2017 and Dean et al 2018 for mineral distribution mapping studies that suggest higher mineral densities in wider, not narrower, cementum increments).

The proportion of collagen fibres emanating from either the cementum or the PDL defines the two major cementum tissue types. Acellular extrinsic fibre

bioRxiv preprint doi: https://doi.org/10.1101/2021.03.25.436951; this version posted March 25, 2021. The copyright holder for this preprint (which was not certified by peer review) is the author/funder, who has granted bioRxiv a license to display the preprint in perpetuity. It is made available under aCC-BY 4.0 International license.

cementum (AEFC) contains predominantly Sharpey's fibres from the PDL. This tissue has the most regular periodicity and provides the most consistent growth record in the cementum. Cellular intrinsic fibre cementum (CIFC) contains only fibres originating from the cementum itself. This tissue grows more sporadically than AEFC with a less precise periodicity and is known to nucleate within regions of the tooth that undergo anomalously high occlusal forcing. As such, AEFC is usually the recommended cementum tissue for cementochronological studies (Naji et al., 2016 and references within).

Several studies have questioned the accuracy, precision and reliability of current methods of imaging and analysing cementum increments (Renz and Radlanski, 2006; Kasetty et al., 2010). Cementum is a dynamic, biomechanically responsive tissue and increments are known to both split and coalesce, which can undermine confidence in their counts as an estimate of age at death. The overwhelming majority of previous studies have relied on thin-sectioning samples to image increments using light microscopy (Naji et al., 2016). This allows increments to be viewed at high spatial resolutions, and offers a range of optical (Stutz, 2002) and digital image processing (Lieberman et al., 1990; Wall-Scheffler and Foley, 2008) methods that filter and highlight increments to varying degrees. However, the destructive nature of thin-sectioning and the restrictive two-dimensional (2D) perspective offered by histological sections limit the understanding of the complex nature of cementum and its increments (Renz and Radlanski, 2006). There is a wide range in the reported accuracy (the proximity of estimated increment counts to known/true chronological age in years) and precision (repeatability and reproducibility between researchers) of increment counts (Lipsinic et al., 1986; Renz

bioRxiv preprint doi: https://doi.org/10.1101/2021.03.25.436951; this version posted March 25, 2021. The copyright holder for this preprint (which was not certified by peer review) is the author/funder, who has granted bioRxiv a license to display the preprint in perpetuity. It is made available under aCC-BY 4.0 International license.

and Radlanski, 2006; Obertová and Francken, 2009), despite generally high reported accuracy and precision across multiple studies (Naji et al., 2016).

Computer vision and image processing have been explored to aid human counting of cementum increments, and to overcome the need for human counting itself (Czermak et al., 2006; Klauenberg & Lagona, 2007). Peaks and troughs in cementum opacity or greyscale 'luminance' can be extracted along radial transects through the cementum from digital micrographs of thin-sections using image processing software and studied by using 'Digital Cementum Luminance Analysis' (DCLA) (Wall-Scheffler and Foley, 2008) (Fig. 2a-b). Light increments are represented by distinct peaks in luminance values, and dark increments by distinct troughs in luminance values (Fig. 2b). These patterns are interpreted by either manually counting peaks and/or troughs, or through peak/trough detection algorithms (e.g. 'Find peaks' in ImageJ/Fiji; Schneider et al., 2012). This abstraction of increments to peaks and troughs offers a less subjective method for manually counting increments, compared to directly reading thin-section images (Fig. 2b). Further, the use of numerical greyscale values to distinguish neighbouring light and dark increments allows quantitative thresholds to be defined for distinguishing increments. These thresholds represent a specific greyscale value from which peaks/troughs representing light/dark increments must differ from either the last trough or peak (respectively), or from the mean value of greyscale for the transect under study, in order to be identified as a 'genuine' increment.

However, DCLA methods have so far relied upon *a priori* assumptions regarding the contrast in greyscale values caused by incrementation versus those caused by other sources such as image noise. The chosen threshold value for distinguishing increments in each DCLA method is specific to the image technique

bioRxiv preprint doi: https://doi.org/10.1101/2021.03.25.436951; this version posted March 25, 2021. The copyright holder for this preprint (which was not certified by peer review) is the author/funder, who has granted bioRxiv a license to display the preprint in perpetuity. It is made available under aCC-BY 4.0 International license.

and hence image data in the original study, and so may not be robustly applied to data from other imaging modalities or techniques, or to taxa that fail to meet the specified threshold specified in the original study. Thus, the next stage in DCLA development should focus on developing a more flexible strategy for distinguishing cementum increments based on relative instead of absolute greyscale distribution criteria.

3D imaging, such as high-resolution computed tomography (CT) using X-ray propagation-based phase-contrast imaging (PPCI) at synchrotron radiation (SR) sources, may overcome the limitations posed by counting cementum increments in histological thin-sections. SR CT has revolutionised the study of other hard tissue microstructures such as vascular and cellular networks in bone (Schneider et al., 2007; Schneider et al., 2009; Sanchez et al., 2012; Goggin et al., 2016; Núñez et al., 2017; Goring et al., 2019) or growth increments in enamel (Tafforeau et al., 2006, 2007; Tafforeau and Smith, 2008; Le Cabec et al, 2015; Green et al., 2017). SR CT imaging of such tissues provides a 3D context to the study of internal structures at sub-micrometre levels, and, with high signal-to-noise ratio (SNR) and high contrast-to-noise ratios (CNRs), provides high levels of image quality. PPCI through SR CT has recently allowed increments to be followed through the cementum of the teeth of archaeological humans (Mani-Caplazi et al. 2017; Newham 2018; Le Cabec et al., 2018) and macaque monkeys and early mammal fossils (Newham 2018; Newham et al. 2020a,b), overcoming the limitations of 2D thin-section-based imaging. The study of Le Cabec et al. (2018) investigated a sample of human teeth from an archaeological population of known age at death, and reported high precision between counts performed by different observers, and for repeated counts performed by the same observer. However, although a strong correlation was found between age estimated by increment counts and known age, the accuracy (proximity of estimated age to known

bioRxiv preprint doi: https://doi.org/10.1101/2021.03.25.436951; this version posted March 25, 2021. The copyright holder for this preprint (which was not certified by peer review) is the author/funder, who has granted bioRxiv a license to display the preprint in perpetuity. It is made available under aCC-BY 4.0 International license.

age) of estimates fell from 2.5 years in individuals 20-29 years old to 28 years in individuals 60-89 years old (with counts consistently underestimating true age). The canines studied in Le Cabec et al. (2019) were not histologically thin-sectioned. On this account, it could not be determined whether the nature of the source of this inaccuracy was biological, diagenetic (chemical changes to the cementum changing and overprinting original increments), or technical (insufficient image contrast between increments due to similar material properties in terms of X-ray interactions and/or due to unsuitable imaging and/or CT reconstruction settings).

Here, we aim to optimise PPCI through SR CT for studying cementum increments in 3D, in comparison with the respective histological data in 2D. We will particularly assess the potential for overcoming the limitations identified in current approaches for counting cementum increments. As a second objective, we provide a validated, semi-automated and robust algorithm for user-independent counting of cementum increments.

2. Materials and Methods

2.1. Teeth samples

This study is focused on the analysis of the right lower first molars (m1) from a sample of 10 female Rhesus macaques (*Macaca mulatta*), raised under laboratory conditions and bred for biomedical research at the Primate Breeding Facility of Public Health England, Salisbury (UK) (Table 1). All animals used here were routinely monitored and checked for primate-borne diseases of risk to humans (including hepatitis B, herpes B and tuberculosis) and were humanely killed using an overdose of pentobarbital, under Home Office establishment licence 70-1707, due to being unfit for breeding or whole-animal scientific procedural use. No animal was killed for

bioRxiv preprint doi: https://doi.org/10.1101/2021.03.25.436951; this version posted March 25, 2021. The copyright holder for this preprint (which was not certified by peer review) is the author/funder, who has granted bioRxiv a license to display the preprint in perpetuity. It is made available under aCC-BY 4.0 International license.

the specific purpose of this study. Once the animals were killed, their lower jaws were mechanically dislocated and removed by Public Health England. Lower jaws were then freeze-stored at -20 °C prior to further tissue preparation. The studied sample was classed as Category B biological waste by the UK government. As no animal was sacrificed or harmed for the purpose of this study, no animal research ethics committee approval was needed.

To prepare specimens, lower jaws were first mechanically cleaned of soft tissue using surgical tools (scalpel, scissors and tweezers). The coronoid and angular processes were then removed using a handsaw. Once prepared, specimens were bathed in tap water in a sealed plastic container, which was stored in a fume cupboard for three weeks (21 days). This procedure was adopted to rot away the periodontal ligament and alveolar soft tissue that could not be mechanically removed. After three weeks, teeth were sufficiently loose within the jaw to be easily removed using surgical pliers. The left and right m1 teeth of all animals were fixed in 10% paraformaldehyde (PFA) solution for 10 days to minimise risk of infection.

Finally, the crowns of all teeth were removed using a Buehler IsoMet® Low Speed precision sectioning saw equipped with an Acuthin™ blade (Buehler Ltd, Lake Bluff, IL, USA). Using the same saw, the anterior and posterior roots of each m1 tooth were mechanically separated and mounted on 2 mm-thick carbon fibre rods (CR200600; Ripmax Ltd, Enfield, UK) cut to 1.5 cm length, using cyanoacrylate super glue.

Chronological age at death in years was known for each individual (Table 1). This data point, and the average age of replacement of lower m1 teeth for captive populations of *Macaca mulatta* (approximately 12-18 months; Bowen and Kock, 1970) provided an expected increment count for each individual. However, a potential

bioRxiv preprint doi: https://doi.org/10.1101/2021.03.25.436951; this version posted March 25, 2021. The copyright holder for this preprint (which was not certified by peer review) is the author/funder, who has granted bioRxiv a license to display the preprint in perpetuity. It is made available under aCC-BY 4.0 International license.

variation of six months for m1 replacement necessitated the use of a minimum expected increment count, and a maximum expected increment count (one increment higher than the minimum expected count) (Table 1).

2.2. X-ray PPCI of cementum

PPCI for this study was performed during a three-day experiment at the TOMCAT beamline of the Swiss Light Source (SLS) (15-18 March 2016). The station at TOMCAT allows the user to control a series of key experimental settings, affecting the image quality of the resulting CT data (Kitchen et al., 2017; Zeller-Plumhoff et al., 2017). The effects of these experimental settings must be systematically assessed in order to achieve optimal experimental conditions for the specific purpose and required image quality of a study.

In a preliminary experiment, the cementum tissue of specimen l56 was imaged using X-ray PPCI through SR CT for a range of different experimental settings. Four key experimental settings (X-ray energy, exposure time, number of X-ray projections, and sample-to-detector distance) were individually varied according to Table 2, while all other experimental settings were fixed at an X-ray energy of 20 keV, a voxel size of 0.66 µm and an exposure time of 150 ms for 1501 projections, at a sample-to-detector distance of 14.00 mm, which corresponds to a similar effective X-ray propagation distance of 13.99 mm (Zeller-Plumhoff et al., 2017) due to the parallel X-ray beam geometry at TOMCAT. The effects of changing experimental settings on image quality of cementum increments were characterised by the signal-to-noise ratio (SNR) and the contrast-to-noise ratio (CNR) as figure of merits. SNR quantifies the level of the image signal relative to the background noise. CNR is a useful measure for assessing image contrast between distinct structures, such as dark/light cementum increments.

bioRxiv preprint doi: https://doi.org/10.1101/2021.03.25.436951; this version posted March 25, 2021. The copyright holder for this preprint (which was not certified by peer review) is the author/funder, who has granted bioRxiv a license to display the preprint in perpetuity. It is made available under aCC-BY 4.0 International license.

Image quality measures for each experimental setting were calculated for 10 CT slices, representing the same regions of the tooth root of l56 in each scan (Fig. 3). SNR was calculated as the ratio between the mean greyscale value (representing density) for a 150-pixel × 150-pixel region of interest (ROI) of cementum ($\overline{g_c}$) and the standard deviation of a 150-pixel × 150-pixel sample of background (i.e. air) (σ_b) in each slice:

$$SNR = \frac{\overline{g_c}}{\sigma_b} \quad (1)$$

CNR was calculated as the difference of the mean greyscale values of the same ROIs of cementum ($\overline{g_c}$) and air ($\overline{g_b}$), respectively, divided by the pooled standard deviation, following the Pythagorean Theorem of Statistics ($Var(X \pm Y) = Var(X) + Var(Y)$ or $\sigma^2(X \pm Y) = \sigma^2(X) + \sigma^2(Y)$ for independent random variables X and Y, with Var and σ denoting the variance and standard deviation, respectively):

$$CNR = \frac{\overline{g_c} - \overline{g_b}}{[(\sigma_c^2 + \sigma_b^2)/2]^{1/2}}, \quad (2)$$

where σ_c and σ_b represent the standard deviations of cementum and background, respectively. Mean values of SNR and CNR were calculated from the values for these 10 slices and compared between all experimental settings (Fig. 4 and Table 2).

Following this preliminary study, an X-ray energy of 20 keV and a sample-to-detector distance of 14 mm was chosen. This provided sufficient image contrast between cementum increments. For each scan, the exposure time was set to 150 ms, and 1501 projections were taken per scan. These settings provided sufficient image quality at scan times that allowed the entire sample to be imaged during our fixed-time experiment. The phase of each X-ray projection was retrieved through the Paganin single-distance non-iterative phase retrieval algorithm, (Paganin et al., 2002), implemented in-house at TOMCAT. The values of the imaginary part of the refractive

bioRxiv preprint doi: https://doi.org/10.1101/2021.03.25.436951; this version posted March 25, 2021. The copyright holder for this preprint (which was not certified by peer review) is the author/funder, who has granted bioRxiv a license to display the preprint in perpetuity. It is made available under aCC-BY 4.0 International license.

index δ=3.7 10^{-8} and the decrement of the real part of the refractive index β=1.7 10^{-10}, and hence the ratio $\delta/\beta = 218$, were fixed for all scans. The phase images were reconstructed using an in-house implementation of the Gridrec algorithm (Marone and Stampanoni, 2012) at TOMCAT. The resulting PPCI CT reconstructions were saved as 16-bit tiff stacks.

2.3. Image processing: straightening and filtering

Image processing of the raw data is often needed before digital image visualisation, segmentation and quantification. This can involve a wide range of image processing methods, the majority of which are based on the manipulation of 2D pixels and/or 3D voxels using mathematical operations (Nixon and Aguado, 2012). Here, we applied two principal image processing methods to individual CT slices: straightening and isolation of cementum, and directional filtering of cementum increments.

For circumferential structures such as cementum increments, it is often difficult to apply standard image processing tools and analyses without distorting results, due to complexities in their patterns and boundaries. Hence, 2D straightening algorithms are often applied in order to further analyse the data. We chose to use the 'Straighten' tool of the open source ImageJ/Fiji image analysis software (Schneider et al., 2012). This tool applies cubic-spline interpolation across a segmented midline of the feature of interest, which is defined by the user. Straightening is then performed using a series of non-linear cubic splines for an arbitrary number of pixels on either side of the midline that can be also be determined by the user. Here, we assigned this number on an individual basis for each dataset, based on the (radial) thickness of cementum being imaged, to ensure that all cementum, but no dentine, was included in the processed image (Fig. 5.a-b). This workflow was then repeated in a semi-automated fashion for all CT slices of each dataset following Newham et al. (2020a),

bioRxiv preprint doi: https://doi.org/10.1101/2021.03.25.436951; this version posted March 25, 2021. The copyright holder for this preprint (which was not certified by peer review) is the author/funder, who has granted bioRxiv a license to display the preprint in perpetuity. It is made available under aCC-BY 4.0 International license.

wherein the same midline coordinates and thickness of the segmentation was applied for as many slices as possible from the first slice of a dataset, before adjusting these parameters once they became suboptimal at several points further through the PPSRCT volume due to misalignment between the scanning and root axes.

Following straightening, cementum datasets were further processed using directional filtering in order to enhance contrast between increments (Fig. 5.d). Filtering is commonly used to suppress the contribution of unwanted signals such as noise, while preserving and enhancing the targeted signal or image contributions for the analysis in question (Freeman and Adelson, 1991). We used a custom MATLAB (R2016a; The MathWorks, Inc., Natick, MA, USA) tool called 'SteerGauss' (version 1.0.0.0) developed and made freely available by Lanman (2006), in order to employ directional Gaussian filtering of straightened cementum images following Freeman and Adelson (1991). For directional Gaussian filtering, a Gaussian function for a set of 2D (x,y) Cartesian coordinates can be prescribed for any arbitrary orientation using a directional derivative operator that interpolates between two 'basic' Gaussian functions, directed at 0° and 90°, respectively. Straightened increments follow similar longitudinal paths, so a steerable filter can be used to select a single orientation of all increments in an image (Fig. 3.c-d). For the current study, the use of a directional Gaussian filter oriented at 90° to the x-axis has been shown to substantially enhance image contrast between straightened cementum increments (see Supplement, section 1. 'Image processing by directional filtering') (Fig. 5).

2.4. Cementum increment counting algorithm

The cementum increment counting algorithm developed here was designed to count cementum increments in a user-independent and semi-automated fashion, further developing the rationale proposed by DCLA for distinguishing individual increments

bioRxiv preprint doi: https://doi.org/10.1101/2021.03.25.436951; this version posted March 25, 2021. The copyright holder for this preprint (which was not certified by peer review) is the author/funder, who has granted bioRxiv a license to display the preprint in perpetuity. It is made available under aCC-BY 4.0 International license.

297 by using a cut-off point that greyscale peaks/troughs must differ by, in order to be
298 counted as a genuine increment. Our algorithm employs population statistics (mean
299 and standard deviation of greyscale values) to count increments, based on the unique
300 distribution of greyscale values within each individual CT slice (see Supplement,
301 section 2 'Robustness testing for increment counting algorithm'). As in DCLA, this
302 method makes use of the average greyscale values along 10 pixel-thick transects through
303 cementum (Fig. 2a). Adapting methods used in tribological surface profiling
304 (Gadelmawla et al., 2002; Esfahani et al, 2018), individual transects are separated into
305 five sections of equal length (Fig. 2b) (see Supplement, section 3 'Splitting of
306 transects through the cementum'). PPCI SR CT datasets of cementum show an
307 overarching reduction in greyscale (density) values from the cemento-dentine
308 boundary to the outer-most cementum increment (Fig. 2a-b) (Newham 2020a,b).
309 Therefore, the use of the mean greyscale value and its standard deviation for the entire
310 transect, as opposed to local values for individual sections of the transect, may
311 preclude the counting of genuine increments towards the outermost increment (as
312 greyscale peaks/troughs are below the mean value), and counting of increments
313 towards the cemento-dentine boundary (as greyscale peaks/troughs are above the
314 mean value). The mean and standard deviation of greyscale values in each section is
315 then calculated (Fig. 2b-d), and light-dark increment pairs are distinguished as peak-
316 trough systems in greyscale that depart from the mean value beyond the local standard
317 deviation in each section (Fig. 2c).

318 Most importantly, this new method for increment counting can be operated in
319 a semi-automated fashion, following an algorithm implemented in the MATLAB
320 statistical environment (see Appendix for MATLAB script). In MATLAB, each
321 individual straightened and filtered cementum image is investigated along a series

bioRxiv preprint doi: https://doi.org/10.1101/2021.03.25.436951; this version posted March 25, 2021. The copyright holder for this preprint (which was not certified by peer review) is the author/funder, who has granted bioRxiv a license to display the preprint in perpetuity. It is made available under aCC-BY 4.0 International license.

of 1000 transects through the cementum chosen at random using a random number generator (Fig. 2a). For each transect, the distance across the transect that the first pixel above zero appears is saved, which gives the radial length of sampled cementum along the transect. Any transect that is less than the lower standard deviation of the saved lengths is then deselected and resampled until all transects fulfil the lower standard deviation of the original sample. Each transect is divided into five sections of equal length (Fig. 2b), and a cubic spline ('Smoothing spline' function in MATLAB) is fitted to the greyscale pattern captured within each section, in order to minimise the influence of image noise on peak/trough patterns (Martinez and Martinez, 2015) (Fig. 2b). For these five smoothed datasets, their mean greyscale value (red lines in Figure 2) is calculated. An upper 'cut-off' value (green lines in Figure 2) is then determined for each section as its mean greyscale value plus half the standard deviation of its greyscale values, and lower 'cut-off' value (blue lines in Figure 2) as the mean greyscale value minus half of the standard deviation. Two new datasets are then created for each section, the first comprised of only greyscale values above the mean, and the other of values below the mean (Fig. 2c). The dataset comprising higher greyscale values thus consists solely of greyscale 'peaks' (local apex in greyscale values), while the dataset comprising lower greyscale values consists solely of greyscale 'troughs' (local nadir in greyscale values) (Fig. 2c). The 'Findpeaks' tool (part of the default 'Signal processing toolbox' in MATLAB) is then used to identify peaks and troughs in their respective datasets (following multiplication with -1 to convert troughs into peaks) and calculate their difference from the mean greyscale value of that section. This allows peaks and troughs that extend beyond the top and bottom cut-off values (respectively) for each section to be identified, providing the first stage of

bioRxiv preprint doi: https://doi.org/10.1101/2021.03.25.436951; this version posted March 25, 2021. The copyright holder for this preprint (which was not certified by peer review) is the author/funder, who has granted bioRxiv a license to display the preprint in perpetuity. It is made available under aCC-BY 4.0 International license.

347 estimating increment and increment pair counts (Fig. 2b-d).

348 Following this first estimate of increment and increment pair counts, further
349 steps are taken within the algorithm to ensure that 'piggy-back' features (secondary
350 peaks/troughs along the ascending/descending limbs of genuine increment peaks
351 and troughs) do not affect increment counts (Fig. 2). No peaks are counted that
352 immediately proceed from the last respective peak; so only one peak is counted for
353 every trough (in Fig. 2c. peaks i and ii are not counted). Also, no peak/trough
354 system along the transect for which each feature is separated by less than three
355 pixels along the transect (or 1.98 µm), are counted, to ensure that grey scale
356 variations on a small scale do not influence increment counts (Fig. 2c peaks i and
357 ii).

358 A final measure is taken to account for increments that are only partly
359 captured inside a neighbouring set of sections along one transect (Fig. 2b-c.). As
360 only the ascending/descending limb of such features would be captured in each
361 section, they may not be detected as a peak/trough in greyscale in either section
362 using the first stage of the increment counting algorithm, which defines peaks or
363 troughs with reference to the two troughs or peaks surrounding them respectively. A
364 second step is therefore undertaken to distinguish, measure and count these features
365 based on their greyscale values relative to the upper and lower standard deviations
366 of each neighbouring section (described in Supplement Section 4 'Accounting for
367 increments split between two neighboring sections'). Once increment pair counts
368 are estimated for the 1000 random transects, the mean and standard deviation are
369 calculated, providing a final estimate of cementum increment pair count.

370 The robustness of the proposed algorithm was tested by applying it to a series
371 of digital sine wave patterns of known increment number between five and 30.

bioRxiv preprint doi: https://doi.org/10.1101/2021.03.25.436951; this version posted March 25, 2021. The copyright holder for this preprint (which was not certified by peer review) is the author/funder, who has granted bioRxiv a license to display the preprint in perpetuity. It is made available under aCC-BY 4.0 International license.

Random noise at different degrees was applied to these patterns in a controlled manner by increasing their standard deviation along the *y*-axis (Fig. 6). Noise was increased incrementally by SNR decrements of 0.1; starting from a SNR of 0.9 and ending at an SNR of 0.1. For each SNR level, increments were counted for 30 sine wave patterns for each count between five and 30. Increment estimates were considered as accurate if the mean estimated count equalled the known increment number to an accuracy of $\pm$ 0.5. Estimates were considered robust for each count as long as the standard deviation for the 30 counted sine wave patterns was < 1, as values above this may produce estimated increment counts of over 1 year above/below known/expected counts (see Supplement Section 2 'Robustness testing for increment counting algorithm').

2.7. Application of cementum increment counting algorithm

The increment counting algorithm presented here was used to generate estimates of increment counts for straightened and filtered CT slices for each lower first molar specimen of the 10 *Macaca mulatta* individuals. We applied the cementum increment counting algorithm to 30 CT slices for each individual, representative of highest cementum increment contrast and quality for each individual (Naji et al., 2016). Each straightened and filtered CT dataset was examined by eye, in order to find the regions of highest increment contrast and minimum amounts of complexity in increment patterns (i.e. splitting and coalescence of increments). 1000 transects were plotted through the cementum in each CT slice, and increment pair counts were generated for each transect. The mean increment pair count for all 1000 transects was then used as the estimated increment pair count for the slice, and the mean count of the 30 slices rounded to the nearest integer was defined as the estimated increment pair count for that *Macaca mulatta* individual.

bioRxiv preprint doi: https://doi.org/10.1101/2021.03.25.436951; this version posted March 25, 2021. The copyright holder for this preprint (which was not certified by peer review) is the author/funder, who has granted bioRxiv a license to display the preprint in perpetuity. It is made available under aCC-BY 4.0 International license.

3. Results

3.1. Optimisation of cementum imaging

When the X-ray energy was changed in isolation, SNR became consistently lower with increasing X-ray energy, whereas CNR peaked at 20 keV, before steadily falling with increasing X-ray energy beyond this point (Fig. 4a). SNR and CNR steadily improved with increasing exposure time (Fig. 4b). SNR and CNR also improved with increased number of projections, although the relative increase in CNR was marginal between 3001 and 4501 projections (Fig. 4c). SNR steadily increased with larger sample-to-detector distances up to 60 mm (Fig. 4d). Whereas CNR steadily rose from 14 mm sample-to-detector distance to a peak at 28 mm, it fell between a sample-to-detector distance of 28 mm and 100 mm (Fig. 4d).

The image quality of the dataset imaged at 28 mm sample-to-detector distance (Fig. 3c) represents an optimum in the trade-off between spatial resolution and contrast for our application. The smoothing inherent in the Paganin phase retrieval algorithm (Zeller-Plumhoff et al., 2017) flattens out increment boundaries and reduces noise, while (mean) greyscale differences are retained between light and dark increments to an extent that offers sufficient image contrast to identify individual cementum increments. For datasets created using smaller sample-to-detector distances (14 mm - 20 mm), high image contrast resulted between increments, but their boundaries were smoothed and less well defined (case Fig. 3b). For sample-to-detector distances above this, the increasing amounts of smoothing diminished the differences in greyscale values between light and dark increments such that by 100 mm sample-to-detector distance, they were difficult to distinguish by eye (case Fig. 3d). This can also be shown quantitatively by plotting greyscale values along transects

bioRxiv preprint doi: https://doi.org/10.1101/2021.03.25.436951; this version posted March 25, 2021. The copyright holder for this preprint (which was not certified by peer review) is the author/funder, who has granted bioRxiv a license to display the preprint in perpetuity. It is made available under aCC-BY 4.0 International license.

422 through the same region of cementum in each dataset (Fig. 3e) acquired at different
423 sample-to-detector distances.

424 *3.2. Cementum imaging results*

425 Cementum was clearly visible in each CT dataset as an incremental tissue wrapping
426 around the dentine of tooth roots and comprising a series of radial increments (Figs. 5
427 and 7-8). The cementum could be distinguished from the dentine due to its
428 significantly lower mean grey values, and the cemento-dentine boundary was marked
429 by the characteristic tissues of the granular layer of Tomes and the high-density
430 hyaline layer of Hopewell Smith (Fig. 7). Individual increments were clearly visible
431 within the cementum and could be followed through the entire dataset, both
432 transversely and longitudinally (Fig. 8).

433 Comparison between CT slices and histological thin-sections of the same
434 regions of cementum (created using the method outlined in Newham et al. (2020a)
435 and imaged using the method outlined in Supplement Section 5 'Thin-section
436 Imaging') suggests that both imaging techniques represent the same cementum
437 increments (Fig. 7). Optical differences between increments in histological data were
438 reflected as grey value differences in CT data. Thick, light increments in histological
439 data corresponded to thick, light increments in CT data, and so absorbed a higher
440 proportion of X-rays relative to thin, dark increments (Fig. 7). Volumetric CT data
441 could further be used to help elucidate primary increments from accessory increments
442 in several specimens. Complexities in increment patterns were witnessed
443 intermittently in every *Macaca mulatta* individual, with individual increments
444 splitting and coalescing to create apparent accessory increments. Following Newham
445 et al. (2020a,b), individual increments could be mapped through the cementum tissue,
446 and the same primary increments could be plotted through the entire scanned tissue

bioRxiv preprint doi: https://doi.org/10.1101/2021.03.25.436951; this version posted March 25, 2021. The copyright holder for this preprint (which was not certified by peer review) is the author/funder, who has granted bioRxiv a license to display the preprint in perpetuity. It is made available under aCC-BY 4.0 International license.

volume (Fig. 8) across these complexities, and distinguished from the accessory increments created. Therefore, regions that were confounded by splitting and coalescing of these increments could be distinguished and excluded for analysis of increment counts (Fig. 8). Also, cellular cementum, the tissue with the least chronological precision in its increment periodicity (Naji et al., 2016), could be distinguished from acellular cementum by the presence of cellular voids, and so could be avoided when identifying high-contrast regions of increments with a circum-annual periodicity (Fig. 7). These two factors, possible due to the entire coronal (crownward) third of the cementum tissue being imaged, led to the identification of the highest quality regions of circum-annual cementum increments for each specimen (Fig. 7).

3.3. Validation of cementum increment counting algorithm

Robustness tests for the proposed increment counting algorithm suggest that it is reliable for SNRs down to 0.2 (Fig. 5). For each simulated pattern of known increment number, the average value of 30 automated counts was identical to the known count for SNRs between 0.9-0.5. The upper/lower standard deviations of these samples did not exceed one integer above/below the known count (Fig. 6). Between SNR levels of 0.5-0.2, average automated counts only differed from known increment number by a value of one in a single sample (with a known increment number of eight). The standard deviations of automated counts exceed one integer above/below the known count for known increment counts of 22 and 28 (Fig. 6). SNRs of 0.1 introduced more errors of between one and two in increment count when compared to the known increment number, and the automated count was outside the region of one standard deviations around the known increment number (Fig. 6).

When increments were algorithmically counted in our macaque data and

bioRxiv preprint doi: https://doi.org/10.1101/2021.03.25.436951; this version posted March 25, 2021. The copyright holder for this preprint (which was not certified by peer review) is the author/funder, who has granted bioRxiv a license to display the preprint in perpetuity. It is made available under aCC-BY 4.0 International license.

compared to expected counts for our sample based on known age, a Spearman's r of 0.77 (p<0.009) and Kendall's τ of 0.71 (p = 0.004) suggest significant correlation between semi-automated increment pair counts and expected numbers of cementum increment pairs. The mean of the semi-automated increment pair counts for each *Macaca mulatta* individual either met the minimum or maximum expected count based on their known age or fell in-between the two for every sample, apart from the juvenile individual t46 whose mean estimated count was 0.5 years more than the maximum expected count (Table 1 and Fig. 9). Juvenile cementum has been previously shown to contain more complex incrementation and greater amounts of increment splitting and coalescence than adult cementum (Klevezal and Stewart, 1994). Standard deviations of increment pair counts (average = 0.83) for the 30 individual CT slices examined for each individual did not exceed one for any *Macaca mulatta* individual. This suggests a precision of within one year for estimated increment counts using the proposed cementum increment counting algorithm.

4. Discussion

4.1. Image quality of SR CT data and optimisation of cementum imaging

The positive relationship observed between both SNR and CNR with increasing exposure time and number of projections has been expected following SR CT imaging of other hard tissues (Tafforeau et al., 2007; Bouxsein et al., 2010). The opposite relationship seen between SNR and X-ray energy can also be explained by a diminished X-ray absorption with increased X-ray energy due to an exponentially decreased probability of photoelectric interactions between X-rays and the tissue. CNR has a more complex relationship with each experimental setting, with an optimum setting at a different level compared to SNR for each experimental setting.

bioRxiv preprint doi: https://doi.org/10.1101/2021.03.25.436951; this version posted March 25, 2021. The copyright holder for this preprint (which was not certified by peer review) is the author/funder, who has granted bioRxiv a license to display the preprint in perpetuity. It is made available under aCC-BY 4.0 International license.

For instance, we located the optimal energy at TOMCAT for cementum increments in terms of CNR at around 20-21 keV, while SNR was highest at 19 KeV and continuously decreased with higher X-ray energies.

The steady increase in SNR with increasing sample-to-detector distance is in agreement with the results of Kitchen et al. (2017), but in contrast to the results of Zeller-Plumhoff et al. (2017). Instead, Zeller-Plumhoff et al. (2017) found that SNR of PPCI SR CT data of muscle tissue steadily decreased when sample-to-detector distance was increased between 30 mm and 60 mm at TOMCAT. The main factors responsible for the increase in SNR with increasing sample-to-detector distance in our study are the steady decrease in the standard deviation of the image background (σ_b) with increasing sample-to-detector distance versus the peak in mean greyscale value of cementum ($\overline{g_c}$) between 28-60 mm (Fig. 4e). The Paganin phase retrieval algorithm acts as a low pass filter, reducing the image noise in the resultant CT reconstructions. This filtering has been enhanced here with increased sample-to-detector and hence propagation distance, as shown by Kitchen et al. (2017). The reason for the different patterns encountered in SNR between the results of Kitchen et al. (2017) and those of Zeller-Plumhoff et al. (2017) were attributed by Zeller-Plumhoff et al. to be due to different targets in terms of image quality, when considering the optimal ratio of δ/β for the Paganin phase retrieval algorithm. The objective of Kitchen et al., and of our study, was primarily to enhance image contrast within the PPCI SR CT data, whereas Zeller-Plumhoff et al. also considered the sharpness of feature boundaries when optimising δ/β. Moreover, the material properties of cementum are different to the soft tissues studied by both Kitchen et al. (2017) (lung tissue) and Zeller-Plumhoff et al. (2017) (muscle tissue).

4.2. X-ray PPCI versus thin-section imaging for counting cementum increments

bioRxiv preprint doi: https://doi.org/10.1101/2021.03.25.436951; this version posted March 25, 2021. The copyright holder for this preprint (which was not certified by peer review) is the author/funder, who has granted bioRxiv a license to display the preprint in perpetuity. It is made available under aCC-BY 4.0 International license.

The first objective of this study was to optimise PPCI through SR CT for studying cementum increments in 3D tomographic data, as an alternative strategy to destructive thin-sectioning and light microscopy for imaging and counting cementum increments. We have shown here that optimised PPCI strategies can overcome the principal caveats of thin-section imaging: namely the destructive sample preparation process and the limited 2D view of tissue that is actually 3D in nature, so lacking context for interpreting complexities in increment patterns; and also limited control over which cementum tissue type is imaged (AEFC versus CIFC). The high image quality offered by SR CT, including phase retrieval offered in PPCI, has provided comparable fidelity for counting individual cementum increments to thin-section histological images of the same regions. The volumetric nature of CT datasets allows navigation through the entire cementum tissue at an isotropic and sub-micrometre nominal spatial resolution. Individual cementum increments can be followed across regions exhibiting complex cementum patterns, created by splitting and coalescence of increments, and regions of CIFC can be avoided when analysing AEFC. This minimises the potential for inaccurate increment counting. As a non-destructive technique the use of PPCI through SR CT for cementochronology permits the study of cementum in specimens previously beyond the reach of traditional histological analyses that are destructive, including fossils (Newham et al., 2020b) and archaeological specimens (Mani-Caplazi et al. 2017; Le Cabec et al., 2019). As there is no physical thin-sectioning of the tissue involved for CT, images are not affected by tissue preparation artefacts such as scratches on the ground and polished thin section or tissue distortion through the mechanical cutting process, which can obscure or alter image details on cementum increments (Czermak et al., 2006; Naji et al., 2016).

bioRxiv preprint doi: https://doi.org/10.1101/2021.03.25.436951; this version posted March 25, 2021. The copyright holder for this preprint (which was not certified by peer review) is the author/funder, who has granted bioRxiv a license to display the preprint in perpetuity. It is made available under aCC-BY 4.0 International license.

546 However, our PPCI of cementum through SR CT has also highlighted the
547 sensitivity of cementum image quality to experimental settings. This suggests that
548 optimisation of experimental settings should be conducted preliminary to every
549 cementochronological PPCI experiment using SR CT, in order to ensure optimised
550 image quality for identifying and counting cementum increments. Optimal
551 experimental settings are specific to the optics of the synchrotron beamline and the
552 material properties, size and morphology of the specimen, and so should be
553 investigated when any of these factors are changed. Also, although CT is generally
554 considered to be non-destructive it became apparent during scanning that micrometre-
555 scale cracks, which are not visible macroscopically, have formed within the
556 cementum tissue (Supplementary Fig. S3) due the interaction of the hard X-rays with
557 the teeth and/or related effects due to this interaction. Although this damage could not
558 be seen macroscopically, it may indicate that further preparation of teeth and/or
559 adaptation of experimental conditions for SR CT imaging is needed, including tissue
560 dehydration and/or cooling (Peña Fernández et al., 2019).

561 *4.3. Cementum increment counting algorithm*

562 The second objective of this study was to provide a validated, semi-automated and
563 robust algorithm for user-independent counting of cementum increments. The manual
564 counting of cementum increments amongst a restricted number of thin-sections per
565 tooth, plays a central role in the current user-dependent approach for counting
566 cementum increments. This subjectivity has led to a wide range of different
567 accuracies and precisions reported for increment counts and their correlation with
568 known age in animal and human samples. Both accuracy and precision in estimated
569 increment counts correlate with the experience of the researcher when compared to
570 known age (i.e. expected increment count) in validation studies (Naji et al., 2016).

bioRxiv preprint doi: https://doi.org/10.1101/2021.03.25.436951; this version posted March 25, 2021. The copyright holder for this preprint (which was not certified by peer review) is the author/funder, who has granted bioRxiv a license to display the preprint in perpetuity. It is made available under aCC-BY 4.0 International license.

Our algorithm offers a new method for objectively counting cementum increments in a user-independent and semi-automated fashion. This substantially decreases the subjectivity and propensity for human error involved in increment counting. Within the same selected sample of straightened, isolated and filtered PPCI slices, our algorithm requires no further human input for counting cementum increments and will estimate the same increment count regardless of the experience of the researcher. The accuracy and precision of this algorithm has been validated here for both simulated data and our experimental sample of *Macaca mulatta* cementum. It could also be further assessed in the same quantitative manner with other PPCI cementum data from animals of known age. Such assessment will allow for further optimisation of our algorithm and tailoring for a wide range of PPCI cementum data.

Finally, although we state the advantages of PPCI imaging over traditional thin-section histological imaging here, the validation of our application on thin-section data of cementum from animals of known age may afford its application for thin-section images. If found to be an accurate method for counting thin-section increments, implementation of our algorithm for thin-sections has potential as an important tool for validating the accuracy of counts estimated by-eye, or even discounting the need for counting increments by-eye completely.

5. Conclusion

In conclusion, we have undertaken a first systematic experimental study on cementum increment counting for non-fossilised dental tissue, based on a comparison between optimised PPCI through SR CT and thin-section histological imaging. Comparison between these two imaging techniques has shown that PPCI SR CT data can provide sufficient spatial resolution and image contrast to reproduce individual growth

bioRxiv preprint doi: https://doi.org/10.1101/2021.03.25.436951; this version posted March 25, 2021. The copyright holder for this preprint (which was not certified by peer review) is the author/funder, who has granted bioRxiv a license to display the preprint in perpetuity. It is made available under aCC-BY 4.0 International license.

increments in the cementum tissue. CT reconstructions are of sufficient quality to count increments semi-automatically using image processing, by defining them as peaks and troughs in greyscale values along transects through the cementum. We have implemented this semi-automated method of increment counting as part of a novel workflow of image processing (cementum isolation, straightening and filtering) and analysis (application of a purpose-built increment counting algorithm). This may help future studies to overcome the central caveat facing current studies of cementum increments: the subjectivity inherent in counting increments by eye that depends on the individual researcher. The combination of non-destructive imaging and objective increment counting may open up a new range of specimens, samples and studies not suitable for destructive thin-section analysis, and help to exploit the potential of cementum as a record of life history for archaeology, anthropology, forensic science and palaeontology.

bioRxiv preprint doi: https://doi.org/10.1101/2021.03.25.436951; this version posted March 25, 2021. The copyright holder for this preprint (which was not certified by peer review) is the author/funder, who has granted bioRxiv a license to display the preprint in perpetuity. It is made available under aCC-BY 4.0 International license.

609 **Acknowledgments and funding:** This study was part-funded by a Natural
610 Environmental Research Council/Engineering and Physical Sciences Research
611 Council doctoral candidateship (UK; grant number NE/R009783/1). Funding was also
612 provided by Ginko Investments Ltd (Bristol, UK), and the Academy of Finland. We
613 acknowledge the Paul Scherrer Institute, Villigen, Switzerland for provision of
614 synchrotron radiation beamtime at the TOMCAT beamline of the SLS (Experiment
615 20151391) and would like to thank Iwan Jerjen, Mark Mavrogordato, Orestis
616 Katsamenis, Sharif Ahmed, Christianne Fernee Juan Núñez, and Priscilla Bayle for
617 their assistance during our beamtime.

618 **Conflict of interest.** The authors report no conflicts of interest.

619 **Author contributions.** EN designed, validated and performed all analyses. All
620 authors were involved in writing the proposal for synchrotron beamtime and
621 synchrotron imaging. All authors contributed to drafting and revising the manuscript.

622 **Data accessibility.** All data supporting this study are openly available from the
623 University of Southampton repository ("https://doi.org/10.5258/SOTON/D1722).

bioRxiv preprint doi: https://doi.org/10.1101/2021.03.25.436951; this version posted March 25, 2021. The copyright holder for this preprint (which was not certified by peer review) is the author/funder, who has granted bioRxiv a license to display the preprint in perpetuity. It is made available under aCC-BY 4.0 International license.

6. References

- Bosshardt DD, Selvig KA. Dental cementum: the dynamic tissue covering of the root. Periodontol. 2000. 1997;13(1):41-75.
- Bosshardt D, Schroeder HE. Evidence for rapid multipolar and slow unipolar production of human cellular and acellular cementum matrix with intrinsic fibers. J. Clin. Periodontol. 1990;17(9):663-668.
- Bosshardt DD, Schroeder HE. Initial formation of cellular intrinsic fiber cementum in developing human teeth. Cell Tissue Res. 1992;267(2):321-335.
- Bouxsein, M. L., Boyd, S. K., Christiansen, B. A., Guldberg, R. E., Jepsen, K. J., Müller, K. J. Guidelines for assessment of bone microstructure in rodents using micro-computed tomography. J. Bone Miner. Res. 2010;25(7):1468-1486.
- Bowen WH, Koch G. Determination of age in monkeys (*Macaca irus*) on the basis of dental development. Lab. Anim. 1970;4(1):113-123.
- Czermak A, Czermak A, Ernst H, Grupe G. A new method for the automated age-at-death evaluation by tooth-cementum annulation (TCA). Anthropol. Anz. 2006;64(1):25-40.
- Esfahani M, Munir KS, Wen C, Zhang J, Durandet Y, Wang J, et al. Mechanical properties of electrodeposited nanocrystalline and ultrafine-grained Zn-Sn coatings. Surf. Coat. Technol. 2018;333:71–80.
- Freeman WT, Adelson EH. The Design and Use of Steerable Filters. IEEE Transactions on Pattern Analysis and Machine Intelligence. 1991;13(9):891–906.
- Frie AK, Fagerheim KA, Hammill MO, Kapel FO, Lockyer C, Stenson GB, et al. Error patterns in age estimation of harp seals (*Pagophilus groenlandicus*): results from a transatlantic, image-based, blind-reading experiment using known-age teeth. ICES J. Mar. Sci. 2011;68(9):1942-1953.

bioRxiv preprint doi: https://doi.org/10.1101/2021.03.25.436951; this version posted March 25, 2021. The copyright holder for this preprint (which was not certified by peer review) is the author/funder, who has granted bioRxiv a license to display the preprint in perpetuity. It is made available under aCC-BY 4.0 International license.

649 • Frie AK, Hammill MO, Hauksson E, Lind Y, Lockyer C, Stenman O, et al. Error
650 patterns in age estimation and tooth readability assignment of grey seals
651 (*Halichoerus grypus*): results from a transatlantic, image-based, blind-reading
652 study using known-age animals. ICES J. Mar. Sci. 2012;70(2):418-430.
653 • Gadelmawla ES, Koura MM, Maksoud TMA, Elewa IM, Soliman HH. Roughness
654 parameters. Journal of materials processing Technology.2002;123(1):133-145.
655 • Geppert EG, Müller KH. Die wurzelzementapposition als meßbarer ausdruck der
656 kaudruckbelastung des zahnes. Dtsch. Zahn Mund Kieferheilkd. Zentralbl.
657 Gesamte. 1951;15:30-119.
658 • Goggin PM, Zygalakis KC, Oreffo RO, Schneider P. High-resolution 3D imaging
659 of osteocytes and computational modelling in mechanobiology: insights on bone
660 development, ageing, health and disease. Eur. Cells and Mater. 2016;31:264-95.
661 • Goring A, Sharma A, Javaheri B, Smith RC, Kanczler JM, Boyde A, et al.
662 Regulation of the bone vascular network is sexually dimorphic. J. Bone Miner.
663 Res. 2019; DOI:10.1002/jbmr.3825.
664 • Grandfield K, Chattah NLT, Djomehri S, Eidelmann N, Eichmiller FC, Webb S,
665 et al. The narwhal (*Monodon monoceros*) cementum–dentin junction: A
666 functionally graded biointerphase. Proceedings of the Institution of Mechanical
667 Engineers, Part H: JIEM. 2014;228(8):754-767.
668 • Green DR, Green GM, Colman AS, Bidlack FB, Tafforeau P, Smith TM.
669 Synchrotron imaging and Markov chain Monte Carlo reveal tooth mineralization
670 patterns. PloS one. 2017;12(10):e0186391.
671 • Immel A, Le Cabec A, Bonazzi M, Herbig A, Temming H, Schuenemann VJ, et
672 al. Effect of X-ray irradiation on ancient DNA in sub-fossil bones–Guidelines for
673 safe X-ray imaging. Sci. Rep. 2016;6:32969.

bioRxiv preprint doi: https://doi.org/10.1101/2021.03.25.436951; this version posted March 25, 2021. The copyright holder for this preprint (which was not certified by peer review) is the author/funder, who has granted bioRxiv a license to display the preprint in perpetuity. It is made available under aCC-BY 4.0 International license.

674 • d'Incau E, Couture C, Maureille B. Human tooth wear in the past and the present:
675 tribological mechanisms, scoring systems, dental and skeletal
676 compensations. Arch. Oral Biol. 2012;57(3):214-229.
677 • Kagerer P, Grupe G. Age-at-death diagnosis and determination of life-history
678 parameters by incremental lines in human dental cementum as an identification
679 aid. Forensic Sci. Int. 2001;118(1):75-82.
680 • Kaifu Y, Kasai K, Townsend GC, Richards LC. Tooth wear and the "design" of
681 the human dentition: a perspective from evolutionary medicine. Am. J. Phys.
682 Anthropol. 2003;122(S37): 47-61.
683 • Kasetty S, Rammanohar M, Raju Ragavendra T. Dental cementum in age
684 estimation: a polarized light and stereomicroscopic study. J. Forensic
685 Sci. 2010;55(3): 779-783.
686 • Kitchen MJ, Buckley GA, Gureyev TE, Wallace MJ, Andres-Thio N, Uesugi K, et
687 al. CT dose reduction factors in the thousands using X-ray phase contrast. Sci.
688 Rep. 2017;7(1):15953.
689 • Klauenberg K, Lagona, F. Hidden Markov random field models for TCA image
690 analysis. Computational Statistics & Data Analysis. 2007;52(2):855-868.
691 • Klevezal G. (1996) Recording structures of mammals. Boca Raton, Florida: CRC
692 Press; 1996.
693 • Klevezal, G., Stewart, B. S. Patterns and calibration of layering in tooth
694 cementum of female northern elephant seals, *Mirounga angustirostris. J.*
695 *Mammal*. 1994;75(2):483-487.
696 • Kvaal SI, Solheim T. Incremental lines in human dental cementum in relation to
697 age. Eur. J. Oral Sci. 1995;103(4):225-230.

bioRxiv preprint doi: https://doi.org/10.1101/2021.03.25.436951; this version posted March 25, 2021. The copyright holder for this preprint (which was not certified by peer review) is the author/funder, who has granted bioRxiv a license to display the preprint in perpetuity. It is made available under aCC-BY 4.0 International license.

698 • Le Cabec A, Tang NK, Ruano Rubio V, Hillson S. Nondestructive adult age at
699 death estimation: Visualizing cementum annulations in a known age historical
700 human assemblage using synchrotron X-ray microtomography. Am. J. Phys.
701 Anthropol. 2019;168(1);25-44.
702 • Le Cabec A, Tang N, Tafforeau P. (2015) Accessing developmental information
703 of fossil hominin teeth using new synchrotron microtomography-based
704 visualization techniques of dental surfaces and interfaces. PloS
705 one. 2015;10(4):e0123019.
706 • Levy G, Mailland ML. Quantitative study of the effect of occlusal hypofunction
707 on periodontal ligament with and alveolar osteoclastic resorption in rats. J. Biol.
708 Buccale. 1980;8(1):17-31.
709 • Lieberman DE. 1993. Life history variables preserved in dental cementum
710 microstructure. Science. 1993;261(5125):1162-1164.
711 • Lieberman DE, Deacon TW, Meadow RH. Computer image enhancement and
712 analysis of cementum increments as applied to teeth of *Gazella gazella*. J.
713 Archaeol. Sci. 1990;17(5):519-533.
714 • Lipsinic FE, Paunovich E, Houston GD, Robison SF. Correlation of age and
715 incremental lines in the cementum of human teeth. J. Forensic Sci.
716 1986;31(3):982-989.
717 • Listgarten MA, Lang NP, Schroeder HE, Schroeder A. Periodontal tissues and
718 their counterparts around endosseous implants. Clin. Oral Implants Res.
719 1991;2(1):1-19.
720 • Lozano M, Bermúdez de Castro JM, Carbonell E, Arsuaga JL. Non- masticatory
721 uses of anterior teeth of Sima de los Huesos individuals (Sierra de Atapuerca,
722 Spain). J. Hum. Evol. 2008;55(4):713–728.

bioRxiv preprint doi: https://doi.org/10.1101/2021.03.25.436951; this version posted March 25, 2021. The copyright holder for this preprint (which was not certified by peer review) is the author/funder, who has granted bioRxiv a license to display the preprint in perpetuity. It is made available under aCC-BY 4.0 International license.

723 • Marone F, Stampanoni M. Regridding reconstruction algorithm for real-time
724 tomographic imaging. J. Synchrotron Radiat. 2012;19:1029-1037.
725 • Martinez WL, Martinez AR. Computational statistics handbook with MATLAB.
726 Boca Baton, Florida: Chapman and Hall/CRC Press; 2015.
727 • Mayo SC, Davis TJ, Gureyev TE, Miller PR, Paganin D, Pogany A, et al. X-ray
728 phase-contrast microscopy and microtomography. Opt. Express.
729 2003;11(19):2289-2302.
730 • Naji S, Colard T, Blondiaux J, Bertrand B, d'Incau E, Bocquet-Appel JP.
731 Cementochronology, to cut or not to cut? Int. J. Paleopathol. 2016;15:113-119.
732 • Newham E. Corfe IJ, Brown KR, Gostling NJ, Gill PG, Schneider P. Synchrotron
733 radiation-based X-ray tomography reveals life history in primate cementum
734 incrementation. J. R. Soc. Interface. 2020a;17(172):20200538.
735 • Newham E, Gill PG, Brewer P, Benton MJ, Fernandez V, Gostling N J, et al.
736 Reptile-like physiology in Early Jurassic stem-mammals. Nat. Commun.
737 2020b;11(1):1-13.
738 • Nixon M, Aguado AS. Feature extraction and image processing for computer
739 vision. Cambridge, Massachusetts: Academic Press; 2012.
740 • Núñez JA, Goring A, Hesse E, Thurner PJ, Schneider P, Clarkin CE.
741 Simultaneous visualisation of calcified bone microstructure and intracortical
742 vasculature using synchrotron X-ray phase contrast-enhanced tomography. Sci.
743 Rep. 2017;7(1):13289.
744 • Obertová Z, Francken M. Tooth cementum annulation method: accuracy and
745 applicability. In Koppe T, Meyer G, Alt KW, Brook A, Dean MC, Kjaer I, et al.
746 editors. Comparative dental morphology Vol. 13. Basel, Switzerland; 2009. p.
747 184-189.

bioRxiv preprint doi: https://doi.org/10.1101/2021.03.25.436951; this version posted March 25, 2021. The copyright holder for this preprint (which was not certified by peer review) is the author/funder, who has granted bioRxiv a license to display the preprint in perpetuity. It is made available under aCC-BY 4.0 International license.

748 • Paganin D, Mayo SC, Gureyev TE, Miller PR, Wilkins SW. Simultaneous phase
749 and amplitude extraction from a single defocused image of a homogeneous
750 object. J. Microsc. 2002;206(1):33-40.
751 • Pena Fernandez M, Dall'Ara E, Kao AP, Bodey AJ, Karali A, Blunn GW, et al.
752 Preservation of bone tissue integrity with temperature control for in situ SR-
753 MicroCT experiments. Materials (Basel). 2018;11(11).
754 • Rolandsen CM, Solberg EJ, Heim M, Holmstrøm F, Solem MI, Sæther BE.
755 Accuracy and repeatability of moose (*Alces alces*) age as estimated from dental
756 cement layers. Eur. J. Wildl. Res. 2008;54(1):6-14.
757 • Sanchez S, Ahlberg PE, Trinajstic KM, Mirone A, Tafforeau P. Three-
758 dimensional synchrotron virtual paleohistology: a new insight into the world of
759 fossil bone microstructures. Microsc. Microanal. 2012;18(5):1095-1105.
760 • Schneider CA, Rasband WS, Eliceiri KW. NIH Image to ImageJ: 25 years of
761 image analysis. Nat. Methods. 2012;9(7):671.
762 • Schneider P, Krucker T, Meyer E, Ulmann-Schuler A. Weber B, Stampanoni M,
763 et al. Simultaneous 3D visualization and quantification of murine bone and bone
764 vasculature using micro-computed tomography and vascular replica. Microsc.
765 Res. Tech. 2009;72(9):690-701.
766 • Schneider P, Stauber M, Voide R, Stampanoni M, Donahue R, Müller R.
767 Ultrastructural properties in cortical bone vary greatly in two inbred strains of
768 mice as assessed by synchrotron light based micro-and nano-CT. J. Bone Miner.
769 Res. 2007;22(10):1557-1570.
770 • Spinage CA. A review of the age determination of mammals by means of teeth,
771 with especial reference to Africa. Afr. J. Ecol. 1973;11(2):165-187.

bioRxiv preprint doi: https://doi.org/10.1101/2021.03.25.436951; this version posted March 25, 2021. The copyright holder for this preprint (which was not certified by peer review) is the author/funder, who has granted bioRxiv a license to display the preprint in perpetuity. It is made available under aCC-BY 4.0 International license.

- Stock SR, Finney LA, Telser A, Maxey E, Vogt S, Okasinski JS. (2017) Cementum structure in Beluga whale teeth. Acta biomater. 2017;4:289-299.
- Stutz AJ. (2002) Polarizing microscopy identification of chemical diagenesis in archaeological cementum. J. Archaeol. Sci. 2002;29(11):1327-1347.
- Tafforeau P, Bentaleb I, Jaeger JJ, Martin C. Nature of laminations and mineralization in rhinoceros enamel using histology and X-ray synchrotron microtomography: potential implications for palaeoenvironmental isotopic studies. Palaeogeogr. Palaeoclimatol. Palaeoecol. 2007;246(2-4):206-227.
- Tafforeau P, Boistel R, Boller E, Bravin A, Brunet M, Chaimanee Y, et al. Applications of X-ray synchrotron microtomography for non-destructive 3D studies of paleontological specimens. Appl. 2006;83(2):195-202.
- Tafforeau P, Smith TM. Nondestructive imaging of hominoid dental microstructure using phase contrast X-ray synchrotron microtomography. J. Hum. Evol. 2008;54(2):272-278.
- von Cramon-Taubadel N. Global human mandibular variation reflects differences in agricultural and hunter-gatherer subsistence strategies. Proc. Nat. Acad. Sci. 2011;108(49):19546–19551.
- Wall-Scheffler CM, Foley RA. Digital cementum luminance analysis (DCLA): a tool for the analysis of climatic and seasonal signals in dental cementum. Int. J. Osteoarchaeol. 2008;18(1):11-27.
- Zander HA, Hürzeler B. (1958) Continuous cementum apposition. J. Dental Res. 1958;37(6):1035-1044.
- Zeller-Plumhoff B, Mead JL, Tan D, Roose T, Clough GF, Boardman RP, et al. Soft tissue 3D imaging in the lab through optimised propagation-based phase contrast computed tomography. Opt. Express. 2017;25(26):33451-33468.

bioRxiv preprint doi: https://doi.org/10.1101/2021.03.25.436951; this version posted March 25, 2021. The copyright holder for this preprint (which was not certified by peer review) is the author/funder, who has granted bioRxiv a license to display the preprint in perpetuity. It is made available under aCC-BY 4.0 International license.

797

798 **Figure captions**

799 **Figure 1. Histological data of rhesus macaque (*Macaca mulatta*) cementum in the**
800 **lower first molar tooth.**

801 (**a**) Reflected light digital micrograph of the cementum tissue under 20×
802 magnification. Cementum (C) is defined as the tissue wrapping around the
803 circumference of the dentine (D), comprising a series of circumferential increments.
804 Blue dashed line highlights a surface scratch created during the thin-sectioning
805 process. (**b**) Detail marked by red dashed box in (**a**) displaying cementum increments
806 in acellular extrinsic fibre cementum, and cellular voids left by cementoblasts in
807 cellular intrinsic fibre cementum (CIFC) under higher resolution (50× magnification).
808 White arrows highlight 'light' increments, blue arrows highlight 'dark' increments,
809 and red arrows highlight cementoblasts. Red bracketed lines highlight cellular intrinsic
810 fibre cementum. Green bracketed line highlights the hyaline layer of Hopewell-Smith,
811 demarcating the cemento-dentine boundary. Scale bar in (**a**) represents 100 μm. Scale
812 bar in (**b**) represents 30 μm.

813

814 **Figure 2. Tomographic cementum increment counting.** (**a**) Straightened, filtered
815 PPCI SR CT image of *Macaca mulatta* cementum. (**b**) Plot of greyscale values along
816 transect highlighted by the 10 pixel-thick coloured band in (**a**) with outer-cementum
817 surface highlighted with orange asterisk and cemento-dentine boundary by red
818 asterisk. Transects are split into five sections. Light/dark increment pairs are
819 distinguished as peak/trough systems in greyscale values, where both the peak and
820 trough depart from the mean greyscale value of that section (red line), beyond the half
821 standard deviations of greyscale values within the section above the mean (green line)

bioRxiv preprint doi: https://doi.org/10.1101/2021.03.25.436951; this version posted March 25, 2021. The copyright holder for this preprint (which was not certified by peer review) is the author/funder, who has granted bioRxiv a license to display the preprint in perpetuity. It is made available under aCC-BY 4.0 International license.

and below the mean (blue line), respectively. (**c**) Sections split into their upper and lower datasets comprising of peaks and troughs in greyscale that exceed beyond the upper and lower standard deviation (respectively). Here, peak/trough pairs are counted, denoted with red numbers. Troughs and peaks that are not counted are denoted in blue numerals, as they either do not exceed the standard deviation of that section or are less than three pixels away from the last respective peak/trough. (**d**) Resulting increment pair counts for each section as seen in (**b**).

Figure 3. SR CT scan of a tooth root and regions for signal-to-noise ratio (SNR) and contrast-to-noise ratio (CNR) calculations. (**a**) One CT slice of the tooth root of *Macaca mulatta* individual l56. Blue box highlights the region of interest for evaluation of background signal from which the mean greyscale value ($\overline{g_b}$) and standard deviation of greyscale values (σ_b) was generated for SNR and CNR calculations (see Equations (1) & (2)). The green box highlights the sampling area for cementum signal from which the mean greyscale value ($\overline{g_c}$) was generated for SNR and CNR calculations. Dashed red boxes indicate regions highlighted of the detail views. (**b**) Detail from region indicated by dashed red boxes in (**a**) from the dataset acquired at 16 mm sample-to-detector distance. (**c**) Detail from the same region from the dataset acquired at 28 mm sample-to-detector distance. (**d**) Detail from the same region from the dataset acquired at 100 mm sample-to-detector distance. (**e**) Plots of greyscale values along transects indicated by dashed lines in (**b-d**), acquired at different sample-to-detector distances. (**a-d**) White scale bars in (**a**) represent 100 µm in the overview image, 30 µm in the detail view highlighted by the red dashed box, and 10 µm in (**b-d**).

bioRxiv preprint doi: https://doi.org/10.1101/2021.03.25.436951; this version posted March 25, 2021. The copyright holder for this preprint (which was not certified by peer review) is the author/funder, who has granted bioRxiv a license to display the preprint in perpetuity. It is made available under aCC-BY 4.0 International license.

847 **Figure 4. SNR and CNR for sweep of experimental settings for PPCI through**
848 **SR CT.** Data shown is from specimen l56. (**a**) SNR (shown in black) and CNR
849 (shown in red) values for different X-ray energies. (**b**) SNR and CNR values for
850 different exposure times. (**c**) SNR and CNR values for different numbers of angular
851 projections. (**d**) SNR and CNR values for different sample-to-detector distances. (**e**)
852 Relationship between the standard deviation of background (σ_b – shown in black)
853 and the mean of cementum signal ($\overline{g_c}$ – shown in red) with increasing sample-to-
854 detector distance.
855
856 **Figure 5. Image processing of PPCI SR CT images of *Macaca mulatta* cementum.**
857 (**a**) One CT slice of specimen l59. (**b**) Detail of CT slice highlighting circumferential
858 cementum increments with midline shown as yellow line. (**c**) Straightened cementum
859 section following the midline highlighted in (**b**). (**d**) Filtered image of (**c**) using a
860 steerable Gaussian filter.
861
862 **Figure 6. Robustness tests for algorithmic increment counts.** (**a**) Counts (black
863 circles) and their standard deviations (green boxes) for incremental sine wave patterns
864 of 5 up to 30 increments with signal-to-noise ratios (SNRs) of 0.9-0.5. Inset: box
865 displaying an example of a 10-increment pattern with an SNR of 0.5. (**b**) Counts and
866 their standard deviations for incremental sine wave patterns of 5 up to 30 increments
867 with SNRs of 0.4-0.2. Inset; box displaying an example of a 10-increment pattern
868 with an SNR of 0.2. (**c**) Counts and their standard deviations for incremental sine
869 wave patterns of 5 up to 30 increments with an SNR of 0.1. Inset: box displaying an
870 example of a 10-increment pattern with an SNR of 0.1.
871

bioRxiv preprint doi: https://doi.org/10.1101/2021.03.25.436951; this version posted March 25, 2021. The copyright holder for this preprint (which was not certified by peer review) is the author/funder, who has granted bioRxiv a license to display the preprint in perpetuity. It is made available under aCC-BY 4.0 International license.

872 **Figure 7. Comparison between histological and CT data.** (**a**) Detail of histological
873 thin-section of the k49 specimen displaying 12 light increments indicated by blue
874 arrows. (**b**) Detail of reconstructed CT slice of the same region as (**a**) displaying 11
875 cementum increments. (**c**) Detail of histological thin-section of the t46 specimen
876 displaying eight light cementum increments. (**d**) Detail of reconstructed CT slice of
877 the same region as (**c**) displaying eight increments. (**e**) Detail of histological thin-
878 section of the l59 specimen displaying 11 light increments. (**f**) Detail of reconstructed
879 CT slice of the same region as (**e**) displaying 11 increments. (**g**) Detail of histological
880 thin-section of the l56 specimen displaying 12 light increments. (**h**) Detail of
881 reconstructed CT slice of the same region as (**g**) displaying 11 increments. (a-h) Black
882 scale bars represent 30 μm. Yellow whiskers highlight the granular layer of Tomes
883 (labelled GLoT); pink dashed whiskers highlight the hyaline layer of Hopewell Smith
884 (labelled HLHS); and red arrows highlight cellular voids within cellular intrinsic fibre
885 cementum. Red dashed circles highlight surface damaged created during thin-section
886 processing.
887
888 **Figure 8. 3D CT data of cementum increments**. Data shown is from specimen k49.
889 (**a**) Straightened and filtered CT slice displaying 10 increment pairs, highlighted with
890 coloured arrows. (**b**) Schematic of detail from **a** highlighted by dashed red box,
891 showing complexities in increment patterns. Increments are given the same colour as
892 their respective arrows in **a**. Instances of splitting are highlighted with dashed red
893 lines, and instances of coalescence by blue dashed lines. (**c**) 3D model of segmented
894 cementum increment patterns plotted through the majority of the root image by PPCI
895 through SR CT. Scale bars represent 100 μm.
896

bioRxiv preprint doi: https://doi.org/10.1101/2021.03.25.436951; this version posted March 25, 2021. The copyright holder for this preprint (which was not certified by peer review) is the author/funder, who has granted bioRxiv a license to display the preprint in perpetuity. It is made available under aCC-BY 4.0 International license.

Figure 9. Comparison between known increment pair counts and those estimated by the proposed cementum increment counting algorithm. PPCI SR CT data shown are from m1 teeth of ten *Macaca mulatta* individuals of known age (see Table 1). Cyan boxes indicate the interquartile range around the mean estimated increment count, indicated by the thick black line. Whiskers represent the extreme lower and upper estimated counts. Blue circles indicate known age of each individual. Red triangles indicate the maximum and inverted green triangles indicate the minimum expected increment count for each individual based on the approximate age-of-eruption of the m1 at 18 months of age in *Macaca mulatta.*

906 **Table 1.**

Specimen	Age (years)	DOB	DOD	Known increment pair count		Estimated increment pair count	
				Minimum	Maximum	Mean	Standard deviation
K49	12	09.04.03	08.04.15	10	11	10	0.95
K91	11.5	06.10.03	10.04.15	9.5	10.5	10	0.81
K23	12	09.03.03	09.04.15	10	11	10	0.89
K24	12	12.03.03	08.04.15	10	11	10	0.96
L10	11	20.02.04	08.04.15	9	10	9.5	0.94
L14	11	26.02.04	10.04.15	9	10	9.75	0.86
T56	11	14.04.04	10.04.15	9	10	10	0.92
L59	11	17.04.04	09.04.15	9	10	9.5	0.71
K16	10.5	16.09.04	09.03.15	8.5	9.5	9	0.52
T46	5.5	11.03.10	07.07.15	3.5	4.5	5	0.94

907

908 **Table 1.** Life history data, known increment pair counts and estimated increment pair counts for each of the 10 female rhesus

909 macaque (*Macaca mulatta*) individuals studied. DOB = date of birth; DOD = date of death. Mean increment pair counts are

910 rounded to the nearest 0.25 years for comparison with known increment pair counts.

bioRxiv preprint doi: https://doi.org/10.1101/2021.03.25.436951; this version posted March 25, 2021. The copyright holder for this preprint (which was not certified by peer review) is the author/funder, who has granted bioRxiv a license to display the preprint in perpetuity. It is made available under aCC-BY 4.0 International license.

911 **Table 2.**

Scan name	Energy (keV)	Exposure time (ms)	Number of projections	Sample-to-detector distance (mm)	Mean SNR	Mean CNR
SO20	19	150	1501	14	187.9	50.7
SO21	20	150	1501	14	123.8	56.9
SO22	21	150	1501	14	112.9	60.8
SO23	22	150	1501	14	82.6	35.5
SO24	26	150	1501	14	72.0	24.5
SO25	20	100	1501	14	118.3	50.7
SO26	20	125	1501	14	124.0	55.4
SO27	20	300	1501	14	177.8	72.3
SO28	20	150	3001	14	245.4	74.5
SO29	20	150	4501	14	252.7	81.5
SO30	20	150	6001	14	300.5	84.9
SO31	20	150	1501	16	142.2	59.0
SO32	20	150	1501	20	152.9	68.9
SO33	20	150	1501	28	185.6	75.2
SO34	20	150	1501	60	179.6	77.8
SO35	20	150	1501	100	247.4	54.9

912

913 **Table 2. Image quality assessments of PPCI SR CT images using different**

914 **experimental settings.** SNR = signal-to-noise ratio; CNR = contrast-to-noise ratio.

Figure 1.

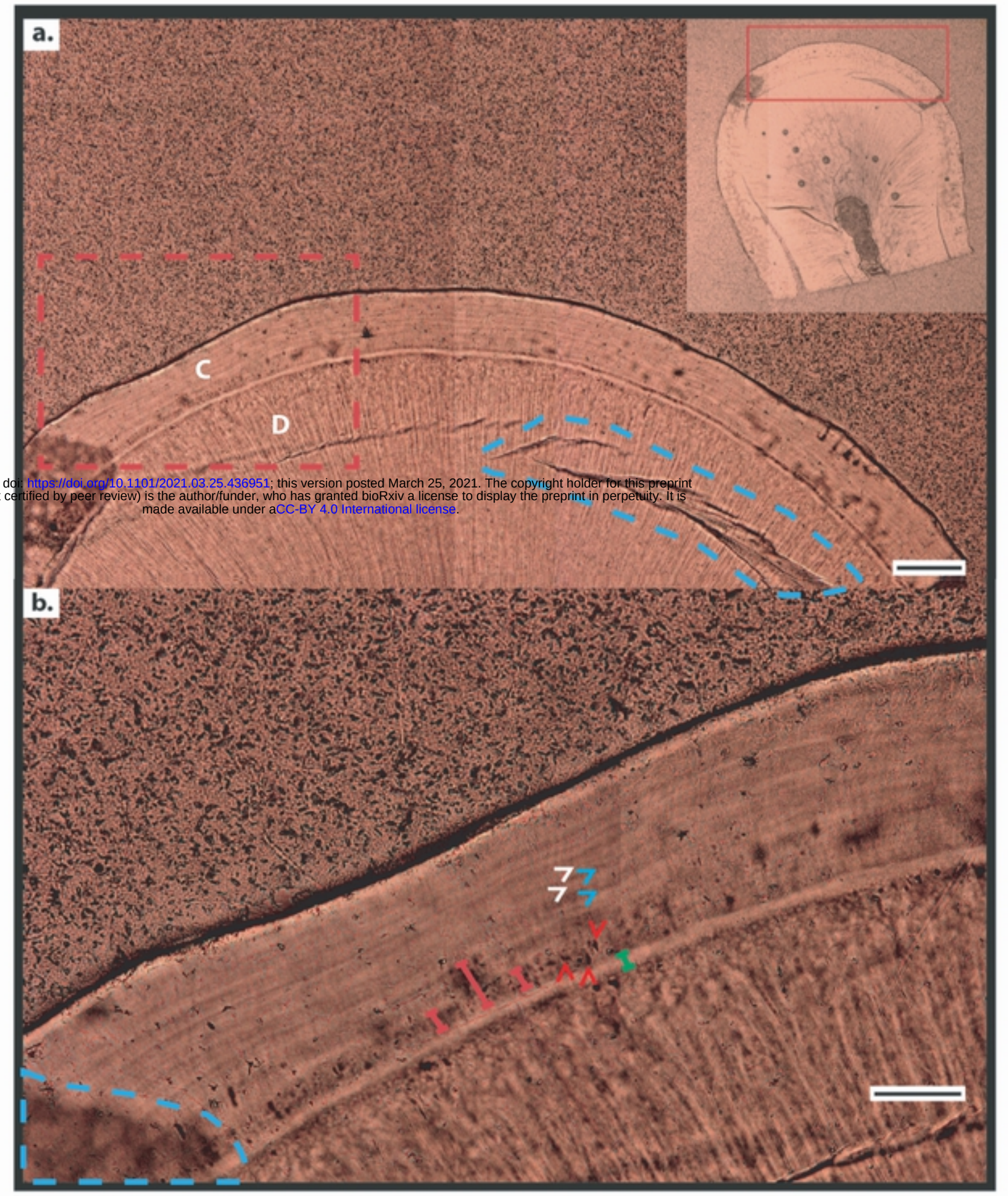

bioRxiv preprint doi: https://doi.org/10.1101/2021.03.25.436951; this version posted March 25, 2021. The copyright holder for this preprint (which was not certified by peer review) is the author/funder, who has granted bioRxiv a license to display the preprint in perpetuity. It is made available under aCC-BY 4.0 International license.

Figure

Figure 3.

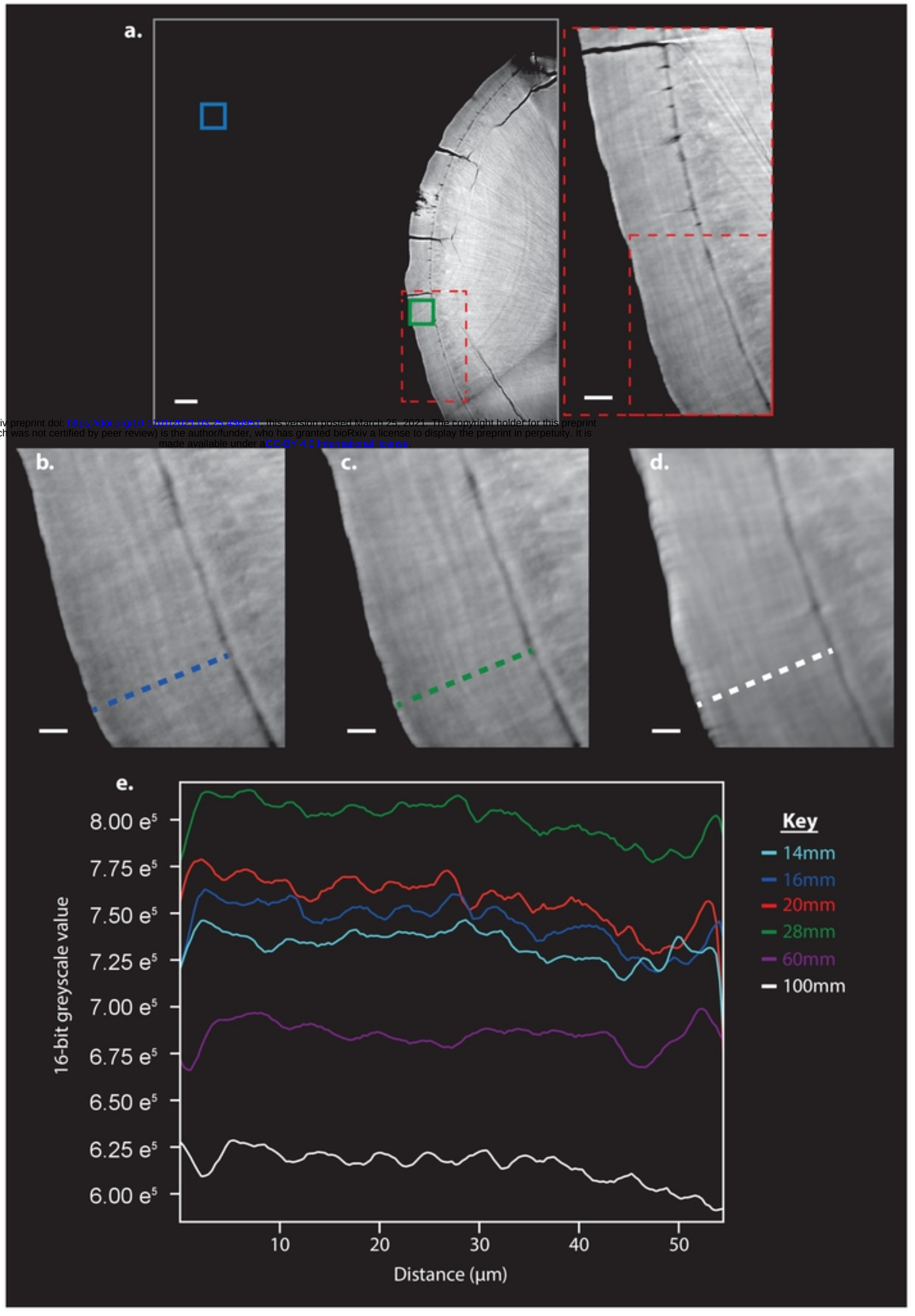

bioRxiv preprint doi: https://doi.org/10.1101/2021.03.25.436951, this version posted March 25, 2021. The copyright holder for this preprint (which was not certified by peer review) is the author/funder, who has granted bioRxiv a license to display the preprint in perpetuity. It is made available under aCC-BY 4.0 International license.

Figure

Figure 4.

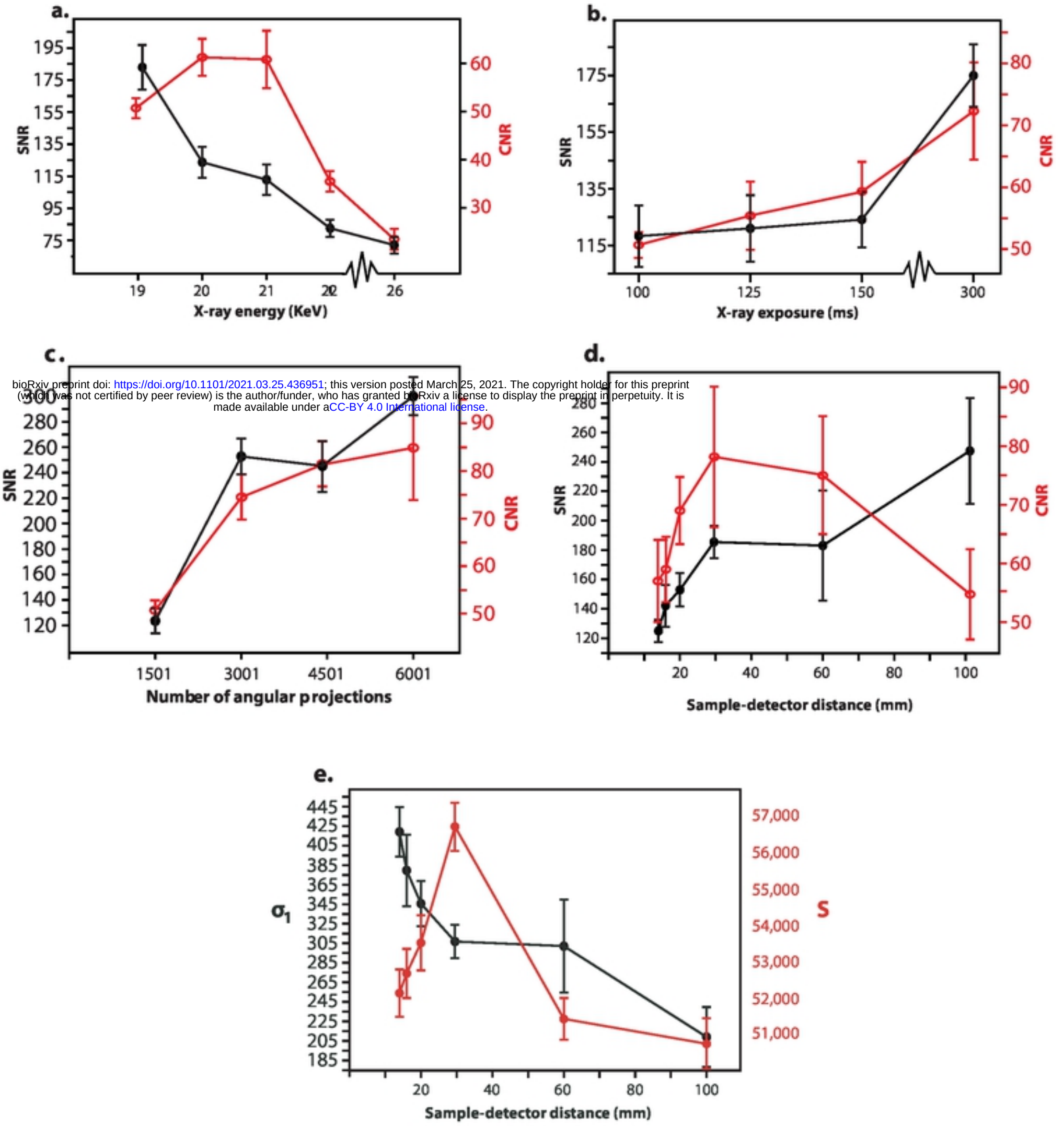

bioRxiv preprint doi: https://doi.org/10.1101/2021.03.25.436951; this version posted March 25, 2021. The copyright holder for this preprint (which was not certified by peer review) is the author/funder, who has granted bioRxiv a license to display the preprint in perpetuity. It is made available under aCC-BY 4.0 International license.

Figure

Figure 5.

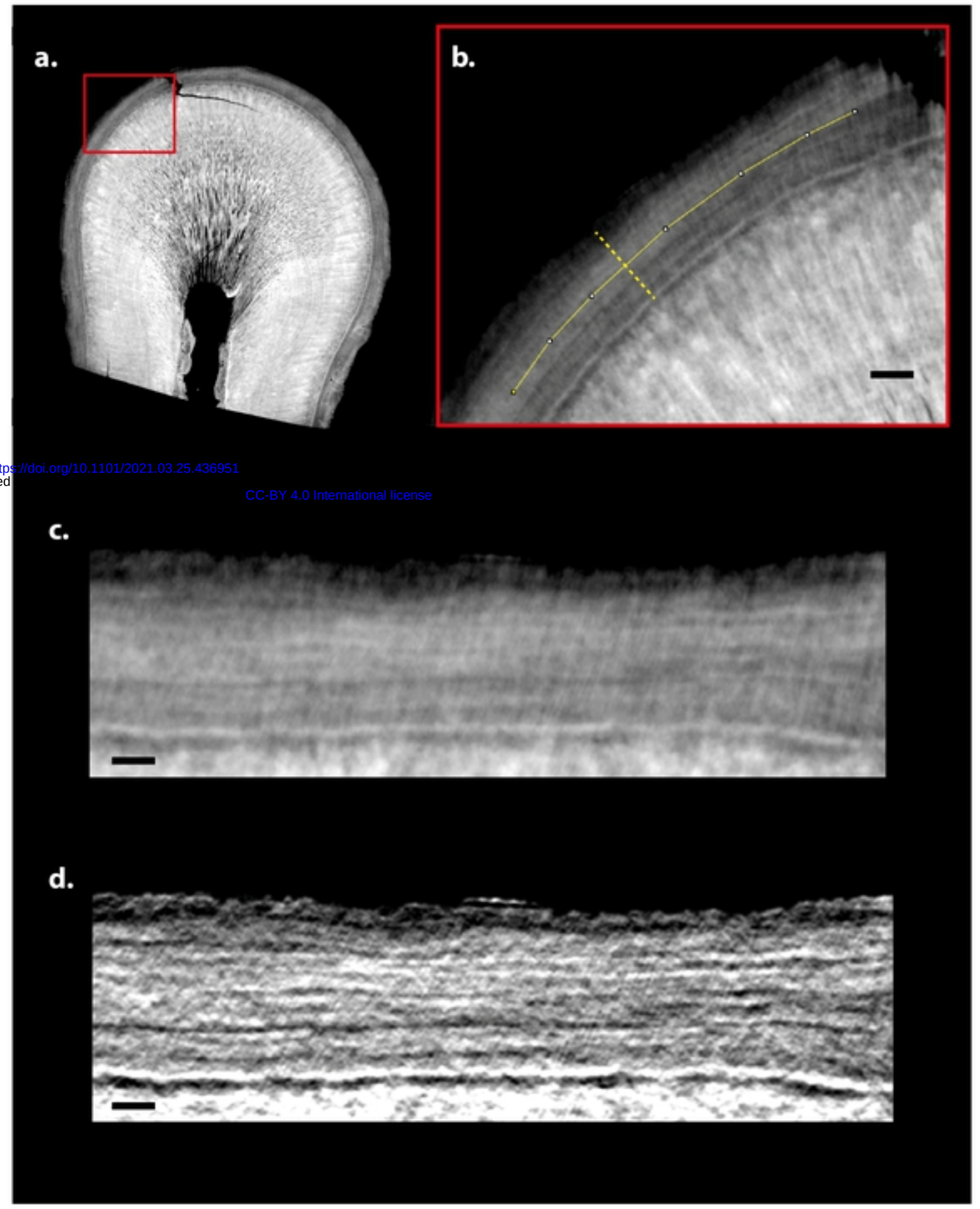

bioRxiv preprint doi: https://doi.org/10.1101/2021.03.25.436951
(which was not certified
CC-BY 4.0 International license

Figure

Figure 8.

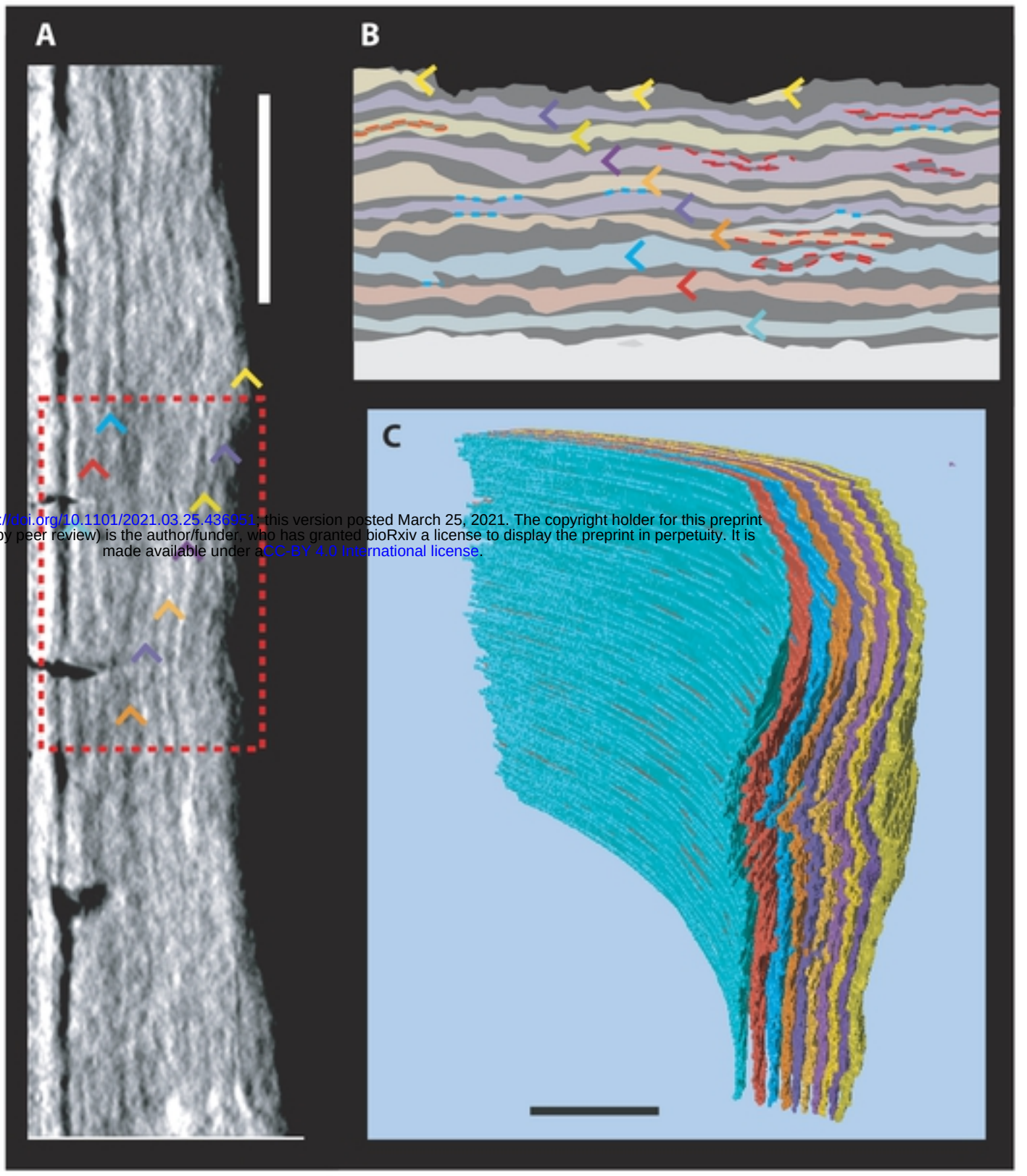

bioRxiv preprint doi: https://doi.org/10.1101/2021.03.25.436951; this version posted March 25, 2021. The copyright holder for this preprint (which was not certified by peer review) is the author/funder, who has granted bioRxiv a license to display the preprint in perpetuity. It is made available under aCC-BY 4.0 International license.

Figure

Figure 2.

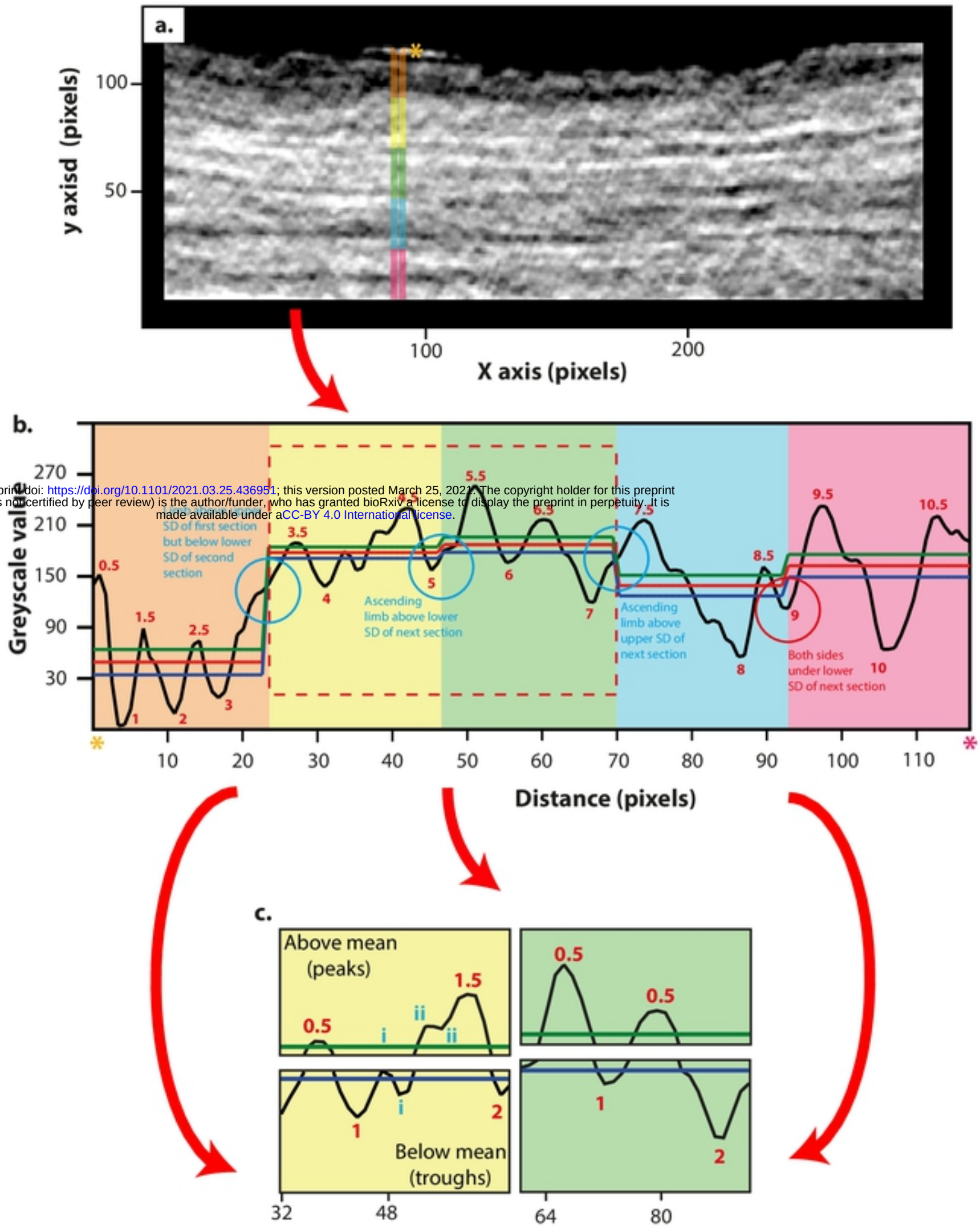

bioRxiv preprint doi: https://doi.org/10.1101/2021.03.25.436951; this version posted March 25, 2021. The copyright holder for this preprint (which was not certified by peer review) is the author/funder, who has granted bioRxiv a license to display the preprint in perpetuity. It is made available under aCC-BY 4.0 International license.

d.

Section	Increment pair count
1	3.0
2	2.0
3	2.0
4	1.5
5	2.0
Total	10.5

Figure

Figure 6.

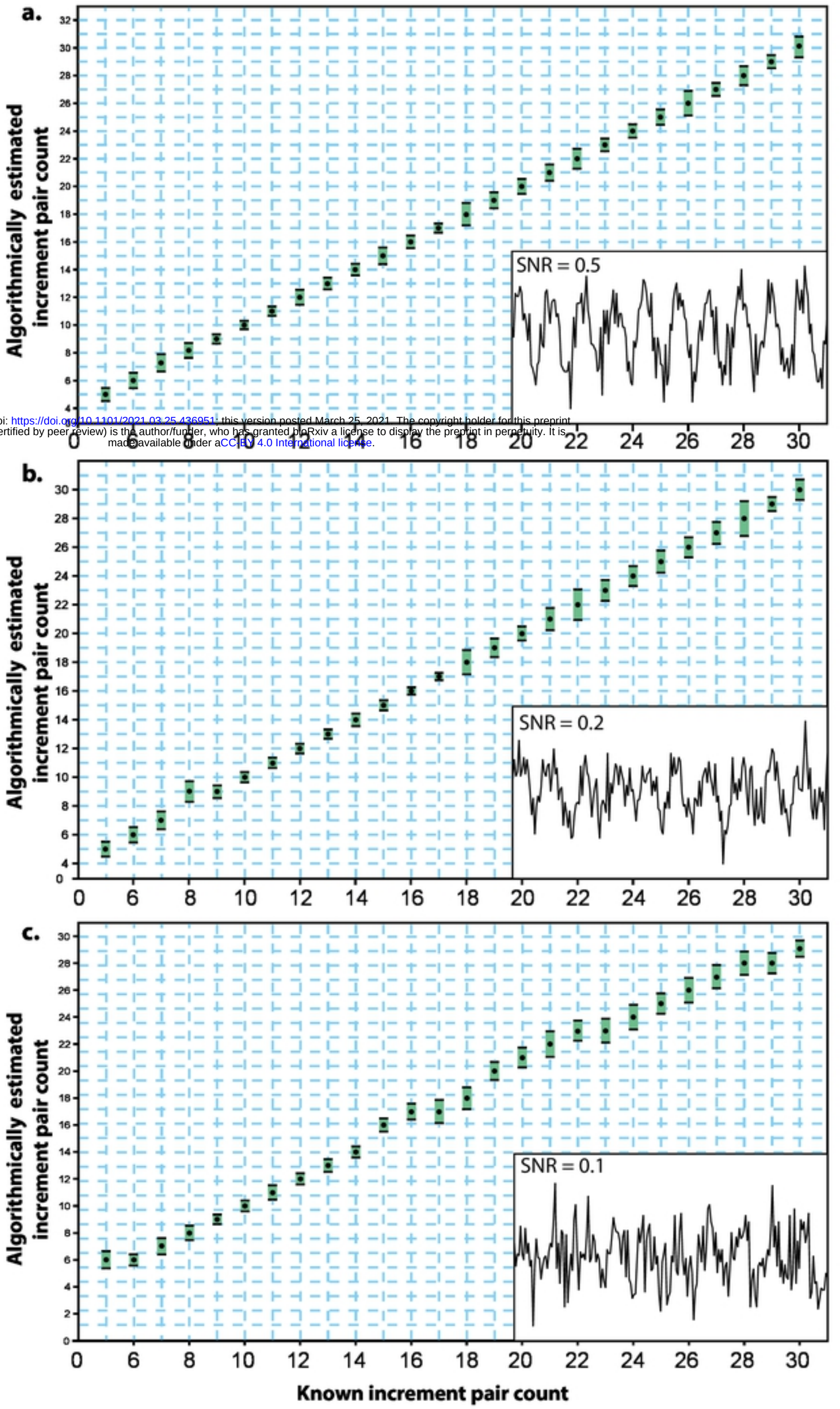

bioRxiv preprint doi: https://doi.org/10.1101/2021.03.25.436951; this version posted March 25, 2021. The copyright holder for this preprint (which was not certified by peer review) is the author/funder, who has granted bioRxiv a license to display the preprint in perpetuity. It is made available under aCC BY 4.0 International license.

Figure

Figure 9.

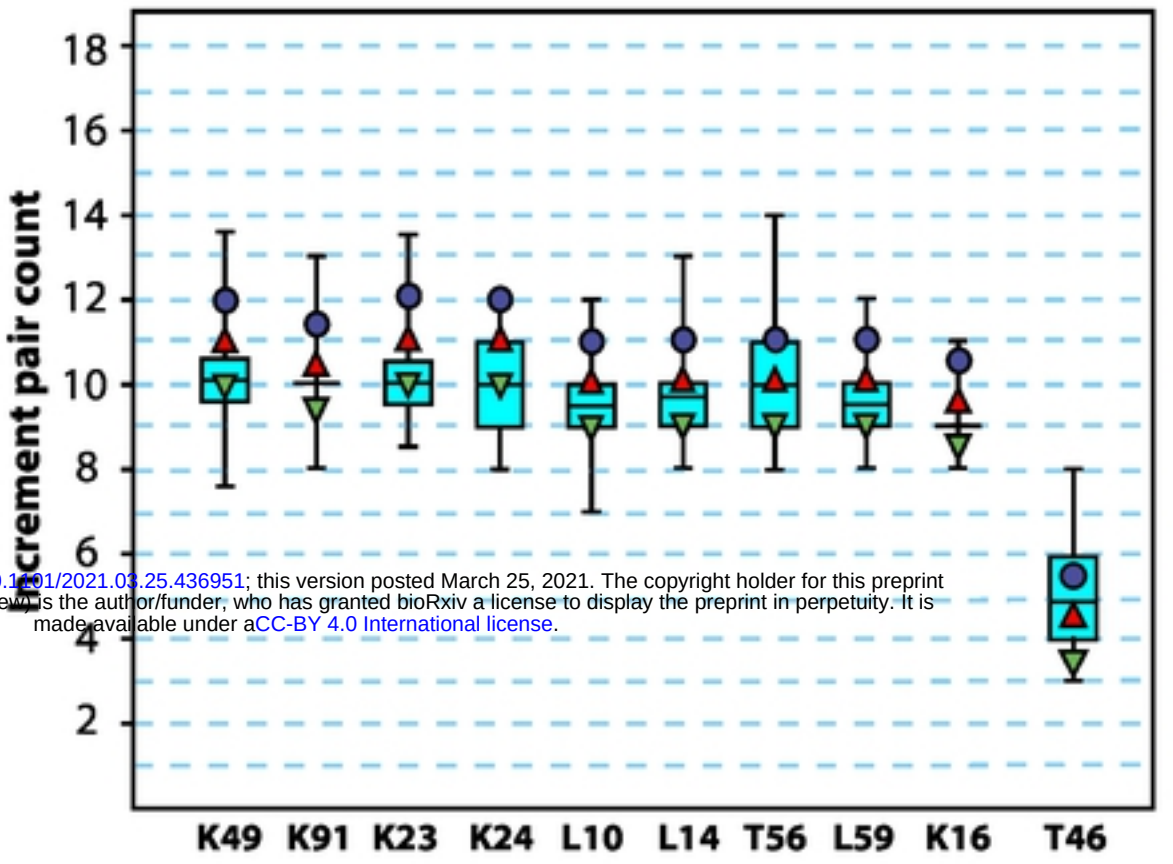

bioRxiv preprint doi: https://doi.org/10.1101/2021.03.25.436951; this version posted March 25, 2021. The copyright holder for this preprint (which was not certified by peer review) is the author/funder, who has granted bioRxiv a license to display the preprint in perpetuity. It is made available under aCC-BY 4.0 International license.

Figure

Figure 7.

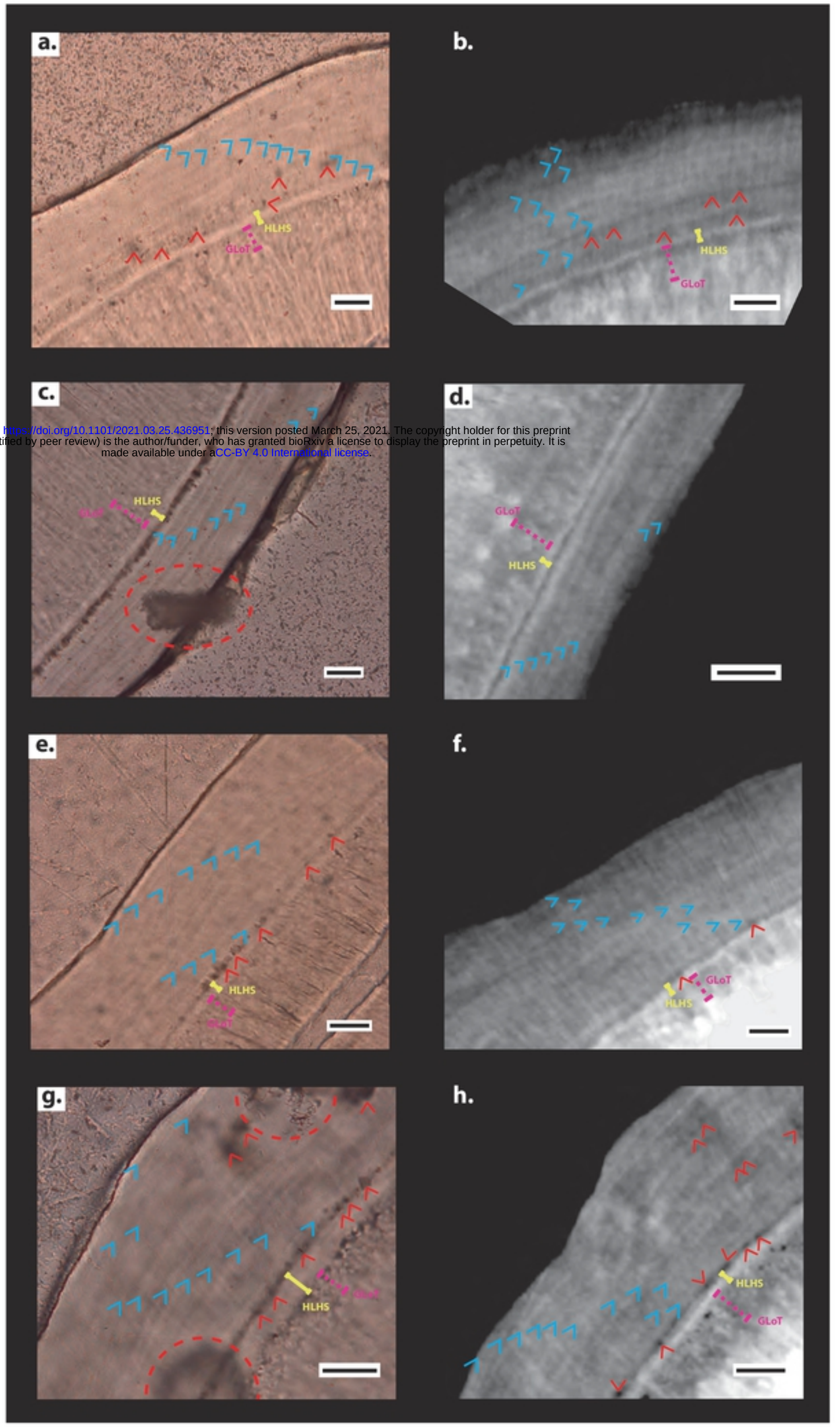

bioRxiv preprint doi: https://doi.org/10.1101/2021.03.25.436951; this version posted March 25, 2021. The copyright holder for this preprint (which was not certified by peer review) is the author/funder, who has granted bioRxiv a license to display the preprint in perpetuity. It is made available under aCC-BY 4.0 International license.

Figure